

## RESEARCH PAPER

# Binary population synthesis of the Galactic canonical pulsar population

Yuzhe Song,<sup>1,2</sup> Simon Stevenson,<sup>1,2</sup> and Debatri Chattopadhyay<sup>3</sup><sup>1</sup>Centre for Astrophysics and Supercomputing, Swinburne University of Technology, Hawthorn, VIC 3122, Australia<sup>2</sup>OzGrav, ARC Centre for Excellence of Gravitational Wave Discovery, Hawthorn, VIC 3122, Australia<sup>3</sup>Gravity Exploration Institute, School of Physics and Astronomy, Cardiff University, Cardiff, CF24 3AA, United Kingdom

Author for correspondence: Y. Song, Email: yuzhesong@swin.edu.au.

## Abstract

Pulsars are rapidly rotating neutron stars that emit radiation across the electromagnetic spectrum, from radio to  $\gamma$ -rays. We use the rapid binary population synthesis suite COMPAS to model the Galactic population of canonical pulsars. We account for both radio and  $\gamma$ -ray selection effects, as well as the motion of pulsars in the Galactic potential due to natal kicks. We compare our models to the catalogs of pulsars detected in the radio, and those detected in  $\gamma$ -rays by *Fermi*, and find broad agreement with both populations. We reproduce the observed ratio of radio-loud to radio-quiet  $\gamma$ -ray pulsars. We further examine the possibility of low spin-down luminosity ( $\dot{E}$ ) pulsars emitting weak, unpulsed  $\gamma$ -ray emission and attempt to match this with recent stacking results. We demonstrate that the apparent correlation between the latitude of a pulsar and its  $\dot{E}$  arises due to natal kicks imparted to pulsars at birth, assuming that all pulsars are born in the Galactic disk.

**Keywords:** Pulsars: general, stars: massive, binaries: general, gamma-rays: general

## 1. Introduction

Pulsars are rotating neutron stars most commonly observed by their periodic radio emission. Around 3500 pulsars are known to date (Manchester et al., 2005). Modern radio facilities such as MeerKAT, ASKAP and FAST are uncovering new pulsars (e.g., Han et al., 2021; Padmanabh et al., 2023), whilst modern search techniques are still discovering pulsars in decades-old archival surveys (e.g., Sengar et al., 2023). The ever-growing pulsar population provides an invaluable insight into the final remnants of massive stellar evolution, whilst relativistic binary pulsars allow for exquisitely precise tests of theories of gravity (e.g., Kramer et al., 2021).

Whilst most pulsars are discovered and studied through radio surveys, some are also observed at other wavelengths, including optical (Cocke et al., 1969; Nather et al., 1969), X-rays (Bradt et al., 1969; Fritz et al., 1969; Oegelman et al., 1993) and  $\gamma$ -rays (Kniffen et al., 1974; Tumer et al., 1984; Thompson et al., 1992). A growing number of pulsars are being detected in  $\gamma$ -rays by the Large Area Telescope (LAT) onboard the *Fermi* space telescope (Smith et al., 2023), including some pulsars which were first detected in  $\gamma$ -rays and then later detected as radio pulsars, a situation exemplified by the Geminga pulsar (Halpern & Holt, 1992; Bertsch et al., 1992; Malofeev & Malov, 1997).

Typically, young pulsars with high spindown luminosity ( $\dot{E}$ ) are found at low Galactic latitudes, and millisecond pulsars (MSPs) are observed in the  $\gamma$ -rays (e.g., Abdo et al., 2009; Abdo et al., 2013; Pletsch et al., 2013; Smith et al., 2023), where  $\dot{E}$  is the spin down luminosity given by

$$\dot{E} = 4\pi^2 \dot{I} P^{-3}, \quad (1)$$

where  $P$  is the spin period of the pulsar,  $\dot{P}$  is its spin derivative

and  $I$  is its moment of inertia. Comparison of the observed  $\gamma$ -ray luminosity  $L_\gamma$  to the spindown luminosity  $\dot{E}$  indicates that  $\gamma$ -ray emission accounts for a large fraction of the energy radiated away by many pulsars (with this fraction  $\eta \gtrsim 10\%$ ; Abdo et al., 2013). Around half of the pulsars detected in  $\gamma$ -rays are also observed in radio, whilst the other half (typically referred to as *radio quiet pulsars*) are not (Abdo et al., 2008; Abdo et al., 2009; Abdo et al., 2013; Smith et al., 2023). The distinction between these two populations likely depends on whether or not their radio emission is beamed towards the Earth (Abdo et al., 2009).

The current sample of  $\gamma$ -ray detected pulsars is around 300 (Abdo et al., 2013; Smith et al., 2019; Smith et al., 2023)<sup>a</sup> and is limited by the sensitivity of *Fermi*-LAT. There is an apparent ‘death-line’ around a spindown luminosity of  $\dot{E} \sim 10^{33} \text{ erg s}^{-1}$ , which may be a result of the limited sensitivity (Abdo et al., 2013). An extensive search of  $\gamma$ -ray pulsations from a thousand pulsars (Smith et al., 2019) provides a similar result that the lack of detection of pulsars with lower  $\dot{E}$  might be due to the limitation of the current instruments, and suggests population synthesis work to explore this specific subpopulation of pulsars.

Recently, Song et al. (2023) performed a stacking analysis of 12 years of *Fermi* data, targeting the positions of 362 known radio pulsars with no previous  $\gamma$ -ray detections. In order to reduce the impact of the Galactic  $\gamma$ -ray background, they selected pulsars that lie at high galactic latitudes ( $|b| > 20^\circ$ ). This probed a population of relatively old, low  $\dot{E}$  pulsars, different to the usual population of  $\gamma$ -ray loud pulsars. Song et al.

<sup>a</sup>A list of *Fermi* detected pulsars is available at <https://confluence.slac.stanford.edu/display/GLAMCOG/Public+List+of+LAT-Detected+Gamma-Ray+Pulsars>

(2023) report the significant detection of  $\gamma$ -rays from this set of pulsars compared to the expected background. Song *et al.* (2023) argue that this suggests that the usual  $\gamma$ -ray death line is predominantly a result of the sensitivity of *Fermi*. In this paper we attempt to explore the implications of this detection for massive binary and pulsar evolution.

Theoretical population synthesis studies can be used to predict the population of observable pulsars under a set of assumptions. There have been several previous population synthesis studies of the  $\gamma$ -ray pulsar population. In a seminal work, Faucher-Giguère & Kaspi (2006) performed a population synthesis of the Galactic radio pulsar population. It accounted for almost all of the relevant effects, including radio selection effects, magnetic field decay and pulsar orbits in the Galaxy. Assumptions were made on distributions of pulsar birth spin period and birth magnetic field strength. Since then, there have been a number of similar studies building on this work (e.g., Takata *et al.*, 2011; Dirson *et al.*, 2022) that include radio and  $\gamma$ -ray selection effect and pulsar evolution theories. Typically, existing pulsar population synthesis works, such as those done by using PsrPopPy (Bates *et al.*, 2014), do not model the details of the full evolution of the binary stellar systems. The study of Kiel *et al.* (2008) is closest to ours in terms of methodology, but they focus on radio pulsars and do not explore the  $\gamma$ -ray pulsar population. In this work, we attempt to explore the canonical radio and  $\gamma$ -ray pulsar populations produced through massive binary stellar evolution. In a follow-up work, we will attempt to understand the full effects on pulsar populations from the stellar evolution physics.

Neutron stars—and hence pulsars—originate from massive stars, and the majority of massive stars are born in binaries (e.g., Sana *et al.*, 2012). Hence, whilst the majority of “normal”, young pulsars (with  $P \gtrsim 0.1$  s) are isolated, most of these objects are expected to have been born in binaries, which are subsequently disrupted by the supernova that formed the neutron star. Hence, the binary fraction and spatial distributions (including scale height) of pulsars encode information about their birth locations and natal kicks. It is then important to account for a full picture of stellar and binary evolution for a better understanding of the Galactic pulsar population. Binary population synthesis code suites, such as COMPAS (Riley *et al.*, 2022), are ideally suited for this task, as they are able to rapidly simulate the evolution of large populations of massive binary stars, incorporating all relevant processes such as natal kicks and pulsar evolution. Understanding the properties of the Galactic pulsar population across the radio and  $\gamma$ -ray wavelengths will aid in constraining pulsar emission physics and the formation and evolution of massive binary stars.

As a first study of the Galactic  $\gamma$ -ray pulsar population using COMPAS, one of the main purposes of this work is to verify the binary and pulsar physics included in COMPAS. This work and its follow-ups can also be used to make predictions for the population of  $\gamma$ -ray pulsars that will be observed in the future with continued operation of *Fermi*-LAT. Other interesting binary pulsar systems include neutron star X-ray binaries (Wijnands & van der Klis, 1998), spider pulsars (Fruchter *et al.*, 1988) and double neutron star binaries (e.g., Hulse &

Taylor, 1975; Abbott *et al.*, 2017), and these events can only be studied through the inclusion of binary physics. In follow-up studies, we will investigate known peculiar binary systems that contain at least one neutron star using COMPAS and other suitable tools.

The remainder of this paper is structured as follows. In Section 2 we describe our methodology. We present our results in Section 3. Section 4 focuses on follow-up studies from this work, and we conclude in Section 5.

## 2. Methods

In this section we introduce the methods and theory used in this study, including evolution theory of isolated pulsars, radio observation and selection criteria, and  $\gamma$ -ray observation and selection criteria. We also introduce the basics of COMPAS relevant to synthesising pulsar populations.

### 2.1 COMPAS

We simulate a population of massive binary stars using the rapid binary population synthesis suite COMPAS (Stevenson *et al.*, 2017; Riley *et al.*, 2022). COMPAS is based on the Single Star Evolution (SSE, Hurley *et al.*, 2000) code and the Binary Star Evolution (BSE, Hurley *et al.*, 2002) code with updates and modifications made. Binary interactions such as mass transfer and common envelope evolution are included, but we neglect the effects of tides (Riley *et al.*, 2022).

We use default binary property parameters for our COMPAS simulations (Riley *et al.*, 2022). These parameters and their values/ranges are based on past theoretical and observational studies. The mass of the initially more massive star in the binary is drawn from an initial mass function (IMF, Kroupa, 2001) within the range of 5 to 150  $M_{\odot}$  as we need stars massive enough to leave behind neutron stars at the end of their evolution. The mass ratio ( $q = m_2/m_1$ ,  $m_2 < m_1$ ) of the binary is drawn from a uniform distribution between 0.01 and 1, with a minimum secondary mass of 0.1  $M_{\odot}$  (Stevenson *et al.*, 2019). We assume initially circular orbits (Hurley *et al.*, 2002). We draw the orbital separation from a uniform distribution in log space with a minimum of 0.01 and maximum of 1000 AU (Sana *et al.*, 2012). Since we are interested in pulsars formed recently in the Milky Way, we assume a representative value of Galactic metallicity  $Z_{\text{Gal}} = 0.014$  (Asplund *et al.*, 2009). A list of default COMPAS option values, including mass transfer rate and common envelope evolution, can be found in the link in footnote<sup>b</sup>.

In this work, neutron stars formed through accretion-induced supernovae, and neutron stars undergoing any recycling/rejuvenation processes are omitted. Only neutron stars formed through core collapse supernovae and electron-capture supernovae that are not in wide, non-interacting binaries (Willcox *et al.*, 2021) are included in the following analysis. The reasoning for this decision is discussed in § 2.2.

<sup>b</sup>[https://github.com/FloorBroekgaarden/Double-Compact-Object-Mergers/blob/main/otherFiles/Table\\_with\\_detailed\\_binary\\_population\\_synthesis\\_simulation\\_settings.pdf](https://github.com/FloorBroekgaarden/Double-Compact-Object-Mergers/blob/main/otherFiles/Table_with_detailed_binary_population_synthesis_simulation_settings.pdf)

## 2.2 Neutron star kicks

Neutron stars receive natal kicks at birth (Lyne & Lorimer, 1994; Hobbs et al., 2005; Verbunt et al., 2017; Igoshev, 2020; Igoshev et al., 2021). We use the physical remnant prescription from Mandel & Müller (2020) to relate the remnant mass and kick of a neutron star to the properties of its progenitor. This prescription is based on semi-analytic supernova models, and is calibrated to the Galactic pulsar population (Kapil et al., 2023); specifically, we use  $v_{\text{NS}} = 520$  km/s for the scaling pre-factor for neutron star kicks, and  $\sigma_{\text{NS}} = 0.3$  for the fractional stochastic scatter in the kick velocities. Kapil et al. (2023) find the distribution of kicks in single and binary neutron stars to be similar, so we opt to use a single distribution for both. As discussed by Mandel & Igoshev (2023), neutron star kicks inferred from young pulsars may be overestimated by  $\sim 15\%$  if pulsar beams are narrow and preferentially aligned with the kick direction. The Mandel & Müller (2020) prescription is applied equally to both core-collapse supernovae and electron-capture supernovae. We do not allow for electron-capture supernovae to occur in wide, non-interacting binaries, to avoid overproducing low-speed pulsars which are not observed (Willcox et al., 2021).

## 2.3 COMPAS Implementation of Pulsar Evolution

This study focuses on canonical pulsars, hence we only describe the evolution of isolated pulsars. Here we follow magnetic braking for an isolated pulsar to spin down, with braking index  $n = 3$ . The pulsar evolution theory implemented in COMPAS is described in Chattopadhyay et al. (2020). We assume an exponentially decaying magnetic field of a neutron star after it spins down for a time duration of  $t$

$$B_f = (B_i - B_{\min}) \exp(-t/\tau) + B_{\min}, \quad (2)$$

where  $B_i$  is the magnetic field strength of the neutron star before it is evolved by time duration  $t$  and  $B_f$  the magnetic field strength afterwards,  $B_{\min}$  is the minimum magnetic field of a pulsar which is set to be  $10^8$  G for the entire analysis, and  $\tau$  is the time scale of pulsar magnetic field decay.

During the time duration  $t$ , the change in the spin period of the neutron star is described as

$$P^2 = \frac{16\pi^2 R^6 \sin^2 \alpha}{3c^3 I} [B_{\min}^2 t - \tau B_{\min} (B_f - B_i) - \frac{\tau}{2} (B_f^2 - B_i^2)] + P_0^2, \quad (3)$$

where  $R$  is the radius of the pulsar (we assume  $R = 10$  km for all pulsars at all times in this work),  $P_0$  is the spin period of the pulsar at the beginning of the evolved time duration  $t$ , and  $B_i$  and  $B_f$  are the pulsar surface magnetic field at the beginning and end of the time step as described in Eq. 2,  $c$  is speed of light,  $\alpha$  is the alignment angle between the magnetic and rotational axes, and

$$I = (0.237 \pm 0.008) m R^2 [1 + 4.2 \frac{M}{M_{\odot}} \frac{\text{km}}{R} + 90 (\frac{M}{M_{\odot}} \frac{\text{km}}{R})^4] \quad (4)$$

being the moment of inertia of the pulsar (Lattimer & Schutz, 2005). Currently in COMPAS,  $\alpha = \pi/2$  is set to be constant

and not evolved (though see Johnston et al., 2020). Evolution of alignment will be included in a future version of COMPAS.

The evolution of period derivative,  $\dot{P}$ , can be described after updating magnetic field strength and spin period, as

$$\dot{P} = \frac{8\pi^2 R^6 B^2 \sin^2 \alpha}{3c^3 I P}, \quad (5)$$

## 2.4 Free Parameters of COMPAS Runs

In addition to the default binary parameters, we need to propose distributions of pulsar properties at birth for subsequent modelling. We note that some of the past population studies (e.g., Faucher-Giguère & Kaspi, 2006; Popov & Turolla, 2012; Szary et al., 2014; Johnston et al., 2020; Chattopadhyay et al., 2020; Dirson et al., 2022; Igoshev et al., 2022) proposed and refined distributions of pulsar properties at birth, such as surface magnetic field strength and spin period. In this work, we also choose the distributions of these two quantities at birth, as well as magnetic decay timescale ( $\tau_d$ ) to be free parameters. By default, COMPAS sets the birth distribution of NS magnetic field as a uniform distribution between  $10^{10}$  G to  $10^{13}$  G, and the birth distribution of NS spin period as a uniform distribution between 10 to 100 ms. These distributions are in general agreement with those observed from young pulsar populations (Manchester et al., 2005). We exclude extremely high magnetic field strengths with  $B > 10^{15}$  G in the magnetar regime as we are uncertain if the magnetar formation and evolution physics would follow those of a normal NS. In our default model, we assume that the magnetic field decay time scale  $\tau_d = 500$  Myr (Chattopadhyay et al., 2021). We choose  $\tau_d$  as a free parameter since there is no clear consensus on whether the magnetic field of a pulsar decays at all, or how long it takes to decay. For example, semi-analytical studies (Gunn & Ostriker, 1970; Vivekanand & Narayan, 1981; Lyne et al., 1985) found that the magnetic field decays on the timescale of the order of a million years, with Dirson et al. (2022) recently finding  $\tau_d = 4.6 \times 10^5$  yr. In comparison, other works (Taylor & Manchester, 1977; Stollman, 1987; Kiel et al., 2008) have shown the opposite, finding that  $\tau_d > 100$  Myr is needed in order for theoretical models to match the observed catalog. For this reason, we let  $\tau_d$  vary from 10 Myr to 1000 Myr in our models.

We list the details of all the models with different pulsar birth distributions and parameters in Table. 1. The initial model (INIT) is as described above. Following that, we vary our model parameters in such ways that we cover different ranges, and in some cases different shapes of the distribution. The D1, D2 and D3 models, combined with INIT, are specifically targeted to examine the impact of the  $\tau_d$  on the results of the simulations, as only  $\tau_d$  is varied in models D1, D2 and D3 compared to INIT. For B1 and B2 models, only the range of the birth magnetic field distributions is changed compared to INIT. Similarly for P1, P2 and P3 models, only the ranges of the birth spin period distributions are changed and the others are kept the same. For PN1, PN2 and PN3 models, the birth spin period distribution is changed to a normal distribution (hence, PN models as in period-normal models) with various

means and standard deviations. In the BLN series of models, the birth magnetic field strength distribution is changed to a log normal distribution, with different means and standard deviations in models BLN1–4. The remaining three models, BLN1–PN1, BLN4–PN1, and BLN1–PN5, have a combination of the magnetic field distribution from the BL models and the spin period distributions of the PN models, respectively. We specifically note that the original form of the log-normal distribution of the birth magnetic field strength is taken from Szary *et al.* (2014). The BLN1–PN5 model is exactly as described in Szary *et al.* (2014). In each COMPAS model, 300,000 binary systems are modelled.

### 2.5 Binary Birth, Pulsar Death, & Parameters

COMPAS begins evolving each binary system at  $T = 0$  Myr. The first stage of post-processing is to assign a birth time of the binary system that corresponds to the Milky Way star formation history. We consider a uniform star formation history of the Milky Way (Vigna-Gómez *et al.*, 2018), enabling us to draw the birth time of the binary systems from a uniform distribution. Without recycling, pulsars rapidly spin down, losing their rotational energy to the point that they can no longer sustain detectable radio or  $\gamma$ -ray emission, at which point we define this as the death of pulsar. The typical characteristic age of a canonical  $\gamma$ -ray pulsar is relatively small, roughly  $10^5$  yrs (Smith *et al.*, 2023). For this reason, we assume that all the neutron stars from the simulation that would potentially be  $\gamma$ -ray emitting are formed in binary systems that are born in the recent history of the Milky Way. The birth time of any given binary system is then drawn from a uniform distribution with a minimum of 12.8 Gyr and a maximum of 13.0 Gyr. We choose to neglect the population of pulsars produced through accretion-induced collapse of white dwarfs as they represent only a small fraction of the population ( $\lesssim 10\%$ ), are formed on much longer timescales and may potentially be born with different properties to those born in core-collapse supernovae (Bailyn & Grindlay, 1990; Tauris *et al.*, 2013).

At this point, the time stamp of the binary system in COMPAS output corresponds to an actual point of time in the history of the Milky Way. We make the observation of any neutron star at the present day, assuming the age of the Milky Way is 13.0 Gyr. If the time stamp is not exactly at 13 Gyr, then a linear interpolation of the two nearest data points is used as the recorded parameter value. COMPAS provides  $P$ ,  $\dot{P}$ ,  $B$  and mass of the neutron star at the observation, and one can estimate the spin-down luminosity via Equation 1.

Before recording the parameters of the neutron star, it is essential to check if the pulsar crosses the radio death-line (Rudak & Ritter, 1994) on the  $P$ - $\dot{P}$  diagram, which is defined by

$$\log_{10} \dot{P} = 3.29 \times \log_{10} P - 16.55, \quad (6)$$

and

$$\log_{10} \dot{P} = 0.92 \times \log_{10} P - 18.65, \quad (7)$$

If  $\dot{P}$  of a neutron star from COMPAS is larger than both of these two calculated values according to Eqs. 6, 7, then the

pulsar has not yet crossed the death-line and may be observable, and we record its parameters. Our treatment of radio selection effects is given in Section 2.7.

### 2.6 Dynamical Evolution

Massive stars, which in later evolutionary stages form neutron stars, are formed within an exponential disk around the Galactic plane. We assume that these massive stars move along their Galactic orbits without any interruption until the change in the evolutionary status of one of the stars in the binary system. As described in § 2.1, we assume all the neutron stars are formed in supernovae. Upon formation, the stellar remnant receives a natal kick as described in § 2.2 which can disrupt the binary system, and in some cases, end up with two individual stars.

Upon the supernova event that forms the neutron star, the binary system is then assigned a random location in the Galaxy following a distribution of a thin, exponential disk (Paczynski, 1990):

$$p_z(z)dz = \exp -z/z_{\text{exp}} \frac{dz}{z_{\text{exp}}}, \quad (8)$$

where  $z$  is the vertical distance from the Galactic plane, and

$$p_R(R)dR = a_R \exp -R/R_{\text{exp}} \frac{R}{R_{\text{exp}}^2} dR, \quad (9)$$

where  $a_R = 1.0683$  and  $R$  is the distance from the Galactic center on the Galactic plane. We set  $z_{\text{exp}} = 75$  pc and  $R_{\text{exp}} = 4.5$  kpc following Paczynski (1990).

Knowing the location of the newly born neutron star, the time at which it is born, and both the magnitude and direction of the natal kick velocity, we can follow its subsequent motion in the Galactic potential. We use NIGO (Rossi, 2015), a numerical galactic orbit integration tool, to evolve the motion of binary systems after the supernova within the Galactic potential. NIGO describes the Milky Way as a disc galaxy, with the Galactic potential comprised of three components: a bulge, a disk and a dark matter halo. The Galactic bulge is described as a Plummer sphere (Flynn *et al.*, 1996; Plummer, 1911):

$$\Phi_b = -\frac{GM_b}{\sqrt{R^2 + z^2 + b_b^2}}, \quad (10)$$

where  $G$  is the gravitation constant,  $M_b = 1.0 \times 10^{10} M_{\odot}$  is the mass of the bulge and  $b_b = 0.4$  kpc is the scale length and  $R^2 = x^2 + y^2$ .

The Galactic disc is modelled by an exponential disc formed by the superposition of three Miyamoto-Nagai potentials (Miyamoto & Nagai, 1975):

$$\Phi_d = -\sum_{n=1}^3 \frac{GM_{d_n}}{\sqrt{R^2 + [a_{d_n} + \sqrt{b_{d_n}^2 + z^2}]^2}}, \quad (11)$$

where  $M_{d_n}$  are the masses of each disk,  $a_{d_n}$  are related to the disk scale lengths of the three disk components (which are



**Table 1.** Description of models used for COMPAS simulations in this work.

Model	$B_{\text{birth}}$ Range (G)	$B_{\text{birth}}$ Distribution	$P_{\text{birth}}$ Range (ms)	$P_{\text{birth}}$ Distribution	$\tau_d$ (Myrs)
Initial	$(10^{10} - 10^{13})$	Uniform	(10 - 100)	Uniform	500
D1	$(10^{10} - 10^{13})$	Uniform	(10 - 100)	Uniform	100
D2	$(10^{10} - 10^{13})$	Uniform	(10 - 100)	Uniform	10
D3	$(10^{10} - 10^{13})$	Uniform	(10 - 100)	Uniform	1000
B1	$(10^{11} - 10^{13})$	Uniform	(10 - 100)	Uniform	500
B2	$(10^{10} - 10^{12})$	Uniform	(10 - 100)	Uniform	500
P1	$(10^{10} - 10^{13})$	Uniform	(10 - 1000)	Uniform	500
P2	$(10^{10} - 10^{13})$	Uniform	(1 - 100)	Uniform	500
P3	$(10^{10} - 10^{13})$	Uniform	(1 - 1000)	Uniform	500
PN1	$(10^{10} - 10^{13})$	Uniform	$\mu = 75, \sigma = 25$	Normal	500
PN2	$(10^{10} - 10^{13})$	Uniform	$\mu = 50, \sigma = 25$	Normal	500
PN3	$(10^{10} - 10^{13})$	Uniform	$\mu = 50, \sigma = 50$	Normal	500
BLN1	$\mu = 10^{12.6}, \sigma = 10^{0.55}$	LogNormal	(10 - 100)	Uniform	500
BLN2	$\mu = 10^{12.0}, \sigma = 10^{0.55}$	LogNormal	(10 - 100)	Uniform	500
BLN3	$\mu = 10^{12.6}, \sigma = 10^{0.25}$	LogNormal	(10 - 100)	Uniform	500
BLN4	$\mu = 10^{12.0}, \sigma = 10^{0.25}$	LogNormal	(10 - 100)	Uniform	500
PN1-B1	$(10^{11} - 10^{13})$	Uniform	$\mu = 75, \sigma = 25$	Normal	500
BLN1-PN1	$\mu = 10^{12.6}, \sigma = 10^{0.55}$	LogNormal	$\mu = 75, \sigma = 25$	Normal	500
BLN4-PN1	$\mu = 10^{12.0}, \sigma = 10^{0.25}$	LogNormal	$\mu = 75, \sigma = 25$	Normal	500
BLN1-PN5	$\mu = 10^{12.6}, \sigma = 10^{0.55}$	LogNormal	$\mu = 300, \sigma = 150$	Normal	500

**Table 2.** Parameters used for the three components of exponential disk

	1	2	3
$M_d$ ( $M_{\odot}$ )	$9.0335 \times 10^{10}$	$-5.9112 \times 10^{10}$	$1.0590 \times 10^{10}$
$a_d$ (kpc)	4.5081	9.6483	1.5136

listed in Table. 2) and  $b_d = 0.2376$  is related to the disk scale height.

An NFW dark matter halo (Navarro et al., 1997) is used in the modelling of the Galactic potential:

$$\Phi_h = -\frac{GM_h}{r} \ln\left(1 + \frac{r}{a_h}\right), \quad (12)$$

where  $M_h = 3.3 \times 10^{12} M_{\odot}$  is the mass of the halo component,  $a_h = 45.02$  kpc is the length scale and  $r^2 = R^2 + z^2$ .

## 2.7 Radio Selection Effects

The observed radio pulsar population represents only a small fraction of the total pulsar population in the Milky Way, and may be strongly biased due to observational selection effects. In this section we describe our modelling of the relevant radio selection effects.

### 2.7.1 Radio Luminosity

One of the primary factors determining whether a pulsar is observable is its radio luminosity. Past population studies have shown that the radio luminosity of a pulsar has no dependency on  $P$  or  $\dot{P}$  of the pulsar itself (Szary et al., 2014). Instead, in the

unit of mJy kpc<sup>2</sup> in 1400 MHz band, it follows a log-normal distribution (Szary et al., 2014)

$$\log L_{1400} \sim N(0.5, 1.0), -3.0 \leq \log L_{1400} \leq 4.0 \quad (13)$$

If a pulsar crosses the “death-line”, described in § 2.5, before the observation is made, then the pulsar is not going to be observed. Additionally, another similar criterion is to examine the radio emission efficiency (Szary et al., 2014) of a pulsar, defined as the fraction of rotational energy transformed into radio emission

$$\xi = \frac{L_r}{E}, \quad (14)$$

where  $L_r$  (erg s<sup>-1</sup>)  $\approx 7.4 \times 10^{27} L_r$  (mJy). As the pulsar ages, its radio emission efficiency will increase. For a pulsar to be detectable in radio,  $\xi < 0.01$  must be satisfied.

### 2.7.2 PSREvolve: Radio Sensitivity

To determine if a pulsar can be observed by a given radio survey, we use the PSREvolve code (Osowski et al., 2011; Chatopadhyay et al., 2020) to calculate the radiometer equation (Dewey et al., 1985; Lorimer & Kramer, 2004) and determine the minimum detectable flux,  $S_{\text{min}}$ , at the sky location at a given signal-to-noise ratio ( $S/N_{\text{min}}$ )

$$S_{\text{min}} = \beta \frac{(S/N_{\text{min}})(T_{\text{rec}} + T_{\text{sky}})}{G \sqrt{n_p t_{\text{int}} \Delta f}} \sqrt{\frac{W_e}{P - W_e}}, \quad (15)$$

where  $T_{\text{rec}}$  and  $T_{\text{sky}}$  are the temperature of the receiver and the direction in the sky, respectively;  $\Delta f$  is the bandwidth of

the receiver,  $G$  is the gain of the telescope,  $n_p$  is the number of polarisations in the detector,  $W_e$  is pulse width and  $P$  is the period of the pulsar, and  $\beta$  is a noise correction factor that increases the noise with digitisation errors and bandpass distortion.

Pulsar detection has been carried out by almost every major radio facility in the world, over a period of more than 50 years, using a variety of different backends. This makes it complicated to individually model each pulsar survey that has been conducted. However, one can focus on modelling some of the largest, most successful surveys (e.g., [Faucher-Giguère & Kaspi, 2006](#); [Graber et al., 2023](#)). In this work, we choose pulsar survey parameters for Equation 15 to represent the Parkes Multibeam Pulsar Survey ([Manchester et al., 2001](#); [Lorimer et al., 2006](#); [Sengar et al., 2023](#)) by setting  $\beta = 1$  and  $S/N_{\min} \geq 10$ . This survey discovered over half of the pulsars detected. Additionally, when comparing the properties of radio pulsars observed by Parkes multibeam surveys and the entire radio pulsar population, the difference in their distributions is negligible, as shown in Fig. 1. For these reasons, we assume that the radio selection is based on a “global” Parkes survey that covers the entire sky, and we use the same specifications as Parkes.

The expression of  $W_e$  below ([Burgay et al., 2003](#)) describes how the ISM impacts the observed pulses. Free electrons in the Galaxy broaden the intrinsic pulses  $W_i$  ([Cordes & Lazio, 2002](#)), and the interstellar medium scatters the pulsar beam.

$$W_e^2 = W_i^2 + \tau_{\text{samp}}^2 + (\tau_{\text{samp}} \frac{\text{DM}}{\text{DM}_0})^2 + \tau_{\text{scatt}}^2, \quad (16)$$

where  $W_i$  is the intrinsic width of the pulse,  $\tau_{\text{samp}}$  and  $\tau_{\text{scatt}}$  sampling and ISM scattering times, DM is the dispersion measure in the direction of the pulsar and  $\text{DM}_0$  is the diagonal dispersion measure of the survey. While the duty cycle of pulsars varies widely, here we assume  $\frac{W_i}{P} = 0.05$  for all pulsars. If the radio luminosity of a pulsar is larger than  $S_{\min} d^2$ , then it can be detected by the chosen radio survey.

### 2.7.3 Radio beaming

Pulsars are considered to be observable during the pulsations, which are strongly beamed. A pulsar should only be observable when the beamed pulsation crosses the line of sight from the Earth. To this end, we should consider the beaming fraction of pulsars in radio, which depends on different emission mechanisms and geometry of the pulsar.

The radio beaming fraction of a pulsar,  $f_r$  ([Tauris & Manchester, 1998](#)), is considered to be

$$f_r = 0.09 \log(P/10)^2 + 0.03,$$

where  $P$  is the rotational period of the pulsar in seconds. We use a probabilistic rejection scheme to use the beaming direction as an additional selection criterion to determine the detectability of pulsars in radio and  $\gamma$ -ray assuming a uniformly distributed viewing angle.

## 2.8 Gamma-ray Selection Effects

### 2.8.1 Gamma-ray Luminosity & Flux

An empirical description of the relationship between the  $\gamma$ -ray luminosity of a pulsar and its physical properties as a fundamental plane has been proposed ([Kalapotharakos et al., 2019, 2022](#)). In this work we estimate pulsar  $\gamma$ -ray luminosity using a fundamental plane in four-dimensional (4D) space that is fitted to 4FGL-DR3 pulsars ([Kalapotharakos et al., 2022](#)),

$$L_\gamma = 10^{14.3 \pm 1.3} E_{\text{cut}}^{1.39 \pm 0.17} B^{0.12 \pm 0.03} \dot{E}^{0.39 \pm 0.05}, \quad (17)$$

where  $E_{\text{cut}}$  is the cutoff energy of a pulsar’s  $\gamma$ -ray SED when modelled by a power-law with the exponential cutoff model,  $B$  is the surface magnetic field strength, and  $\dot{E}$  is the spin-down luminosity. Pulsar  $\gamma$ -ray spectral parameters, cutoff energy  $E_{\text{cut}}$  and power-law index before cutoff  $\Gamma$ , are determined following Figs. 10 & 11 in [Kalapotharakos et al. \(2022\)](#). These two figures show correlations between  $E_{\text{cut}}$  and  $\dot{E}$  and  $\Gamma$  and  $\dot{E}$  respectively when the pulsar has  $10^{33} \text{ erg/s} < \dot{E} < 10^{38} \text{ erg/s}$ . Within this  $\dot{E}$  range, we assume a power-law correlation of  $E_{\text{cut}}$  (in GeV) with  $\dot{E}$  as well as  $\Gamma$  with  $\dot{E}$  with these following correlations

$$\log_{10} E_{\text{cut}} = \log_{10} 0.5 + 0.26(\log_{10} \dot{E} - 33) + U(0.05),$$

and

$$\Gamma = 0.5 + 0.3(\log_{10} \dot{E} - 33) + U(0.05),$$

where  $U(0.05)$  is a random number drawn from a uniform distribution between  $-0.05$  and  $0.05$ . When  $\dot{E} < 10^{33} \text{ erg/s}$ , we set

$$\log_{10} E_{\text{cut}} = \log_{10} 0.5 + U(0.05),$$

and

$$\Gamma = 0.5 + U(0.05).$$

When  $\dot{E} > 10^{38} \text{ erg/s}$ ,  $\log_{10} E_{\text{cut}} = 1.0 + U(0.05)$ ,  $\Gamma = 0.5 + U(0.05)$ .

We can then determine the pulsar’s energy flux by

$$F_\gamma = \frac{L_\gamma}{4\pi d^2 c_g},$$

where  $d$  is the distance of the pulsar to the Earth and  $c_g$  is the flux correction factor ([Watters et al., 2009](#)), which depends on the emission mechanism of the pulsar as well as geometry and viewing angle. Here we combine results from [Johnston et al. \(2020\)](#) and [Pétri \(2011\)](#), and assume that  $c_g$  follows a sigmoid function versus  $\dot{E}$  with a maximum of 0.8 ([Johnston et al., 2020](#)) and a minimum of 0.22 ([Pétri, 2011](#)), while turning over at  $10^{33} \text{ erg s}^{-1}$  with an added randomisation drawn from a uniform distribution between  $-0.1$  and  $0.1$ .

### 2.8.2 Gamma-ray Sensitivity

The 12-year *Fermi*-LAT Source Catalog provides an all-sky map of the detection threshold for the catalog<sup>c</sup>. By comparing

<sup>c</sup>[https://fermi.gsfc.nasa.gov/ssc/data/access/lat/12yr\\_catalog/detthresh\\_PLR3\\_12years\\_PL22.fits](https://fermi.gsfc.nasa.gov/ssc/data/access/lat/12yr_catalog/detthresh_PLR3_12years_PL22.fits)

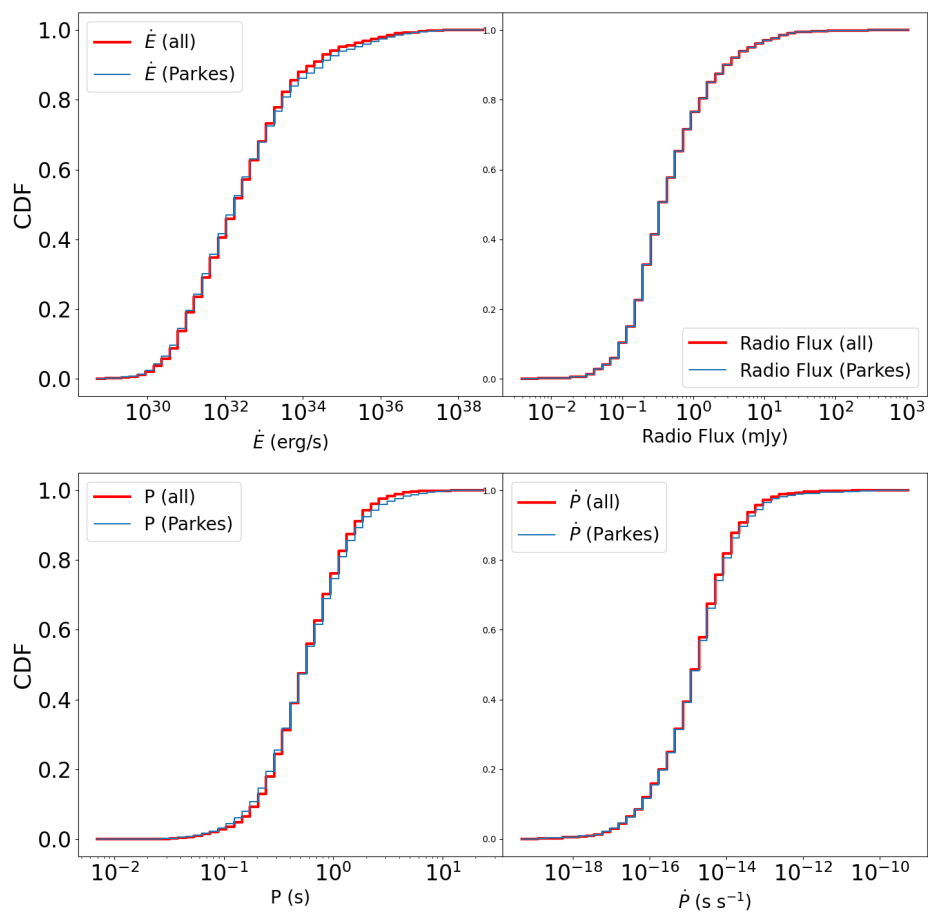


**Figure 1.** Cumulative distribution functions (CDFs) of  $\dot{E}$ , radio flux, period and  $\dot{P}$  of all radio pulsars in the catalogs (red) and pulsars observed in the Parkes Multibeam Surveys (blue).

the energy flux of a pulsar in the simulation to the detection threshold at the corresponding sky location, we would be able to determine if the simulated pulsar would be detectable or not.

In reality, pulsars that are already detected in radio surveys first are easier to find in  $\gamma$ -rays when compared to  $\gamma$ -ray blind searches (Abdo *et al.*, 2013; Smith *et al.*, 2023). Fig. 17 of Abdo *et al.* (2013) clearly indicates that for the detected pulsars in the 2nd *Fermi*-LAT pulsar catalog, pulsars that are already detected in radio in general are easier to detect. For this reason, we make the detection threshold five times lower at the location of the pulsar if the simulated pulsar is detected in radio selection; and 1.5 times higher at the location of the pulsar if the simulated pulsar is not detected in radio.

### 2.8.3 Gamma-ray beaming

Gamma-ray pulsars have a beaming effect similar to that of radio pulsars. In Johnston *et al.* (2020), a description of young and energetic (with  $\dot{E} > 10^{35}$  erg/s) pulsars'  $\gamma$ -ray beaming fraction ( $f_g$ ) is in their Table. 3. We adopt this description in determining the beaming fractions of our modelled pulsars. As this work does not provide a beaming fraction for pulsars with  $\dot{E} < 10^{35}$  erg/s, here we assume that as  $\dot{E}$  decreases, the beaming fraction also decreases. The choices of beaming fraction can be described as

$$f_g = \begin{cases} 0.92, & \text{if } \dot{E} > 10^{38} \text{ erg s}^{-1} \\ 0.82, & \text{if } 10^{37} < \dot{E} \leq 10^{38} \text{ erg s}^{-1} \\ 0.67, & \text{if } 10^{36} < \dot{E} \leq 10^{37} \text{ erg s}^{-1} \\ 0.50, & \text{if } 10^{35} < \dot{E} \leq 10^{36} \text{ erg s}^{-1} \\ 0.40, & \text{if } 10^{33} < \dot{E} \leq 10^{35} \text{ erg s}^{-1} \\ 0.30, & \text{if } \dot{E} \leq 10^{33} \text{ erg s}^{-1} \end{cases}$$

The assumptions above are made based on observations and outer gap model of young, powerful pulsars (Johnston *et al.*, 2020). According to Pierbattista *et al.* (2012), this choice can be dependent on the pulsar emission model and is consistent with what we have chosen.

We also use a probabilistic rejection scheme same as that described in § 2.7.3 similarly for radio pulsars. If beaming is considered in the chosen emission mechanism of the  $\gamma$ -ray pulsar in the simulation, then it is used as an additional selection criterion to determine the detectability of this pulsar in  $\gamma$ -ray, while also assuming a uniformly distributed viewing angle.

### 2.9 Reusing COMPAS Output

Depending on the model parameters, roughly 30% to 50% of binary systems would produce at least one neutron star in each COMPAS simulation. However, due to the selection effects introduced above, only an extremely small portion of these simulated neutron stars are recorded as observable. Adhering to the principle of effectively utilising the simulation, we develop a scheme to reuse each model. Each time the simulation is re-used, the birth time and location of a neutron star is re-assigned. We then make the star travel through the Galactic potential

described above, and make the observation again at 13 Gyr, with re-assigned radio and  $\gamma$ -ray luminosity. This re-using scheme is applied 9 times to each simulation, and along with the original simulation, it is equivalent to 3,000,000 binary systems simulated in each COMPAS model.

## 3. Results & Discussions

The results from the COMPAS simulations using the setups from § 2 are presented in this section, as well as the discussion on the implications of these results. The results are compared to the pulsar catalog to determine the goodness of the different models. This will help us determine the model of pulsar initial conditions that best fits both the radio and  $\gamma$ -ray observations. We will first show the results of the simulation by comparing the number of different types of pulsars produced in different simulation models, then employ a statistical method to compare the distribution of pulsar physical properties to those reported in the catalogs. We further discuss the impact of the results from the selection effects of  $\gamma$ -ray pulsars. We also aim to provide some insights into the  $\gamma$ -ray emission of low  $\dot{E}$  pulsars.

### 3.1 Star Formation Rate

In COMPAS simulations produced for this study, only stars within the initial mass range of  $5 M_\odot$  to  $150 M_\odot$  are modelled. Because of this setup, we need to account for the low-mass end of the initial mass function (IMF) when calculating the star formation rate. Since all the models in this study use the same parameters for binary population, they all have the same star formation rate. Using the *CosmicIntegration* Python package in COMPAS, we are able to account for the lower end of the IMF. By default, we use a Kroupa (2001) broken power-law IMF, with a slope of 0.3 between  $0.01 M_\odot$  and  $0.08 M_\odot$ ; slope of 1.3 between  $0.08 M_\odot$  and  $0.5 M_\odot$ ; slope of 2.3 between  $0.5 M_\odot$  and  $200 M_\odot$ . Each binary system generated in any given COMPAS run corresponds to  $234 M_\odot$  of star formation. Considering we set all the binary systems to be born in the most recent 200 Myr, and each COMPAS output is sampled 10 times, the star formation rate is  $\sim 1.2 M_\odot$  per year with the current model selection. The observed star formation rate over the most recent history of the Milky Way is around  $1.65 \pm 0.19$  (Licquia & Newman, 2015) or  $1.9 \pm 0.4 M_\odot \text{ yr}^{-1}$  (Chomiuk & Povich, 2011). Other works, such as Evans *et al.* (2022), estimate the Milky Way star formation rate in the range of  $0.50 - 5.93 M_\odot \text{ yr}^{-1}$ . The star formation rate from our COMPAS simulations is consistent with these observed and modelled values.

### 3.2 Results

The most straightforward and obvious way to determine if a COMPAS model is a good fit for the observation is to compare the number of pulsars produced by the model to different catalogs. We examine, for each model, the number of radio pulsars, the number of  $\gamma$ -ray pulsars, the number of radio-quiet  $\gamma$ -ray loud pulsars, and the number of radio-loud  $\gamma$ -ray quiet pulsars, produced in the simulation. To fully eliminate the possible randomness from the models, the observation part



of post-processing is repeated 10 times, and the average and standard deviation of these realisations are recorded for each model in Table. 3.

We then tabulate the difference of numbers of pulsars in Table. 4. For many of the models, the predicted number of pulsars is largely different from the observed pulsars. For example, models INIT and D1 have 26% differences in radio pulsars, and 21% and 18% differences in  $\gamma$ -ray pulsars, respectively. An even more extreme case is B2 model, with 7.5 times of radio pulsars and 3.8 times of  $\gamma$ -ray pulsars predicted compared to the observed populations. Due to these large differences, we scale the predicted numbers according to the radio pulsar population. For each model, the numbers of all types of pulsars are scaled by the factor  $N_R/2715$ , with 2715 is the number of observed radio pulsars from the catalogs. These scaled numbers of  $\gamma$ -ray pulsar, radio-quiet and radio-loud  $\gamma$ -ray pulsars, and radio-loud  $\gamma$ -ray-quiet pulsars are then compared to those from the catalogs to calculate the percent difference. The B1 and PN1-B1 models are not scaled as the predicted numbers of radio pulsars are already close to the observed value. Scaling the number of pulsars in a model effectively changes the modelled star formation rate. We scale the default star formation rate of  $1.2M_\odot/\text{yr}$ , as described in § 3.1, by the same scaling factor for each model, to obtain the appropriate number as listed in the last column in Table. 4. Another indicator of the goodness of the models is the ratio between different types of pulsars. Here we check the ratio between radio and  $\gamma$ -ray pulsars, and ratio between radio-quiet and radio-loud  $\gamma$ -ray pulsars for each model, and compare them to those from the catalogs. The percent differences between these predicted and observed ratios are also listed in Table. 4. Both the INIT and PN1-B1 models are able to reproduce the observed numbers and ratios of different types of pulsars to within  $\approx 10\%$ .

Beyond simply comparing the total number of pulsars between observations and our simulations, we can also compare the predicted and observed distributions of various physical quantities of the pulsar populations between the catalog and the simulations. We first plot the cumulative distribution functions (CDFs) for each pulsar parameter for each of the models listed in Table 1 in Figure 2, and compare them to the observed distributions. In general, some of the COMPAS model results produce distributions in most physical quantities that match the observations. But there are a few quantities that cannot be reproduced by any of the COMPAS models (e.g.,  $\gamma$ -ray flux).

Next, we use statistical tests to examine how well the predicted parameter distributions match the observed distributions for each physical quantity. Given that the simulation and catalog have different-sized samples on each quantity, and the quantity of each pulsar should be independent of each other, we use Mann-Whitney U test (MWU test; Mann & Whitney, 1947) to make the comparison. The MWU test is chosen because it is a nonparametric test independent of underlying distributions. The null hypothesis is that both the predicted and observed samples are drawn from the same underlying distribution. Given the model and simulation have different size, and there is no certain theory on the shape of the distribution of each parameter, it is important to use a statistical test

that is independent of the distribution itself. We record the  $p$ -value of the test for a given physical quantity between the comparison of simulation and catalog. If  $p < 0.05$ , it means we reject the null hypothesis that the two compared samples are drawn from the same distribution. When  $p > 0.05$ , we cannot reject the null hypothesis, which means we consider the two distributions to be the same.

In Table. 5, the  $p$ -values of the MWU test for a selection of physical quantities of the pulsars compared between each model and the catalog are shown. For each model, the  $p$ -values shown in Table. 5 are determined from the random realisation of the model shown in Fig. 2. We note a few of the prominent features in this table below:

1. None of the given models can reproduce the distribution of  $\dot{P}$  of radio pulsars. While the CDFs of radio pulsar  $\dot{P}$  look similar between the catalog and some of the models as shown in Fig. 2, the MWU  $p$ -values are always zero.
2. None of the given models can reproduce the distributions of radio flux. This is surprising, as the distribution of radio luminosities that we assume is based on radio observations (Szary et al., 2014). This is likely due to the fact that the models we explored in this study do not cover a larger or fine enough grid within the parameter space, which is unlike some of the commonly used Bayesian analysis methods or machine learning (Graber et al., 2023; Ronchi et al., 2021) that can explore a larger range of the parameter space with the ability to comb through different parts finely. It is likely that a slightly different choice of radio luminosity distribution would yield a better fit to the flux distribution since this is not something that we varied in our models. Additionally, the catalog is made up of pulsars from various pulsar surveys, which each individually would pose different selection effects on the radio pulsar population. In our work, we only chose to implement selection effects based on the Parkes multi-beam pulsar survey (cf. Section 2.7.2), and this should also have an impact on the resulting radio flux distribution.
3. Similarly for  $\gamma$ -ray flux, all of the models report a MWU test  $p$ -value of 0. When examining the CDFs of the  $\gamma$ -ray flux (e.g. in Fig. 3), we find that the simulated  $\gamma$ -ray flux of the pulsars peaks at a lower value compared to those of the catalog. This effect is to some level expected as the changes from the sensitivity level mean that our simulation might be sensitive to  $\gamma$ -ray pulsars with lower flux. Given that the difference in the peak value is roughly a factor of 2, we think this is an acceptable result as it is important to keep the selection of  $\gamma$ -ray sensitivity as described above to reflect the observations. Additionally, a recent conference abstract (Tabassum & Lorimer, 2024) suggested that the 3D fundamental plane might not work well for  $\gamma$ -ray pulsars. As described in § 2.8.1, we use 3D fundamental plane in this work to model the  $\gamma$ -ray luminosity of pulsars. This might also cause problem in matching model to the catalogs.
4. Only one model, which is the PN1-B1 model, is able to reproduce the period distribution of radio pulsars that resemble that of the catalog.

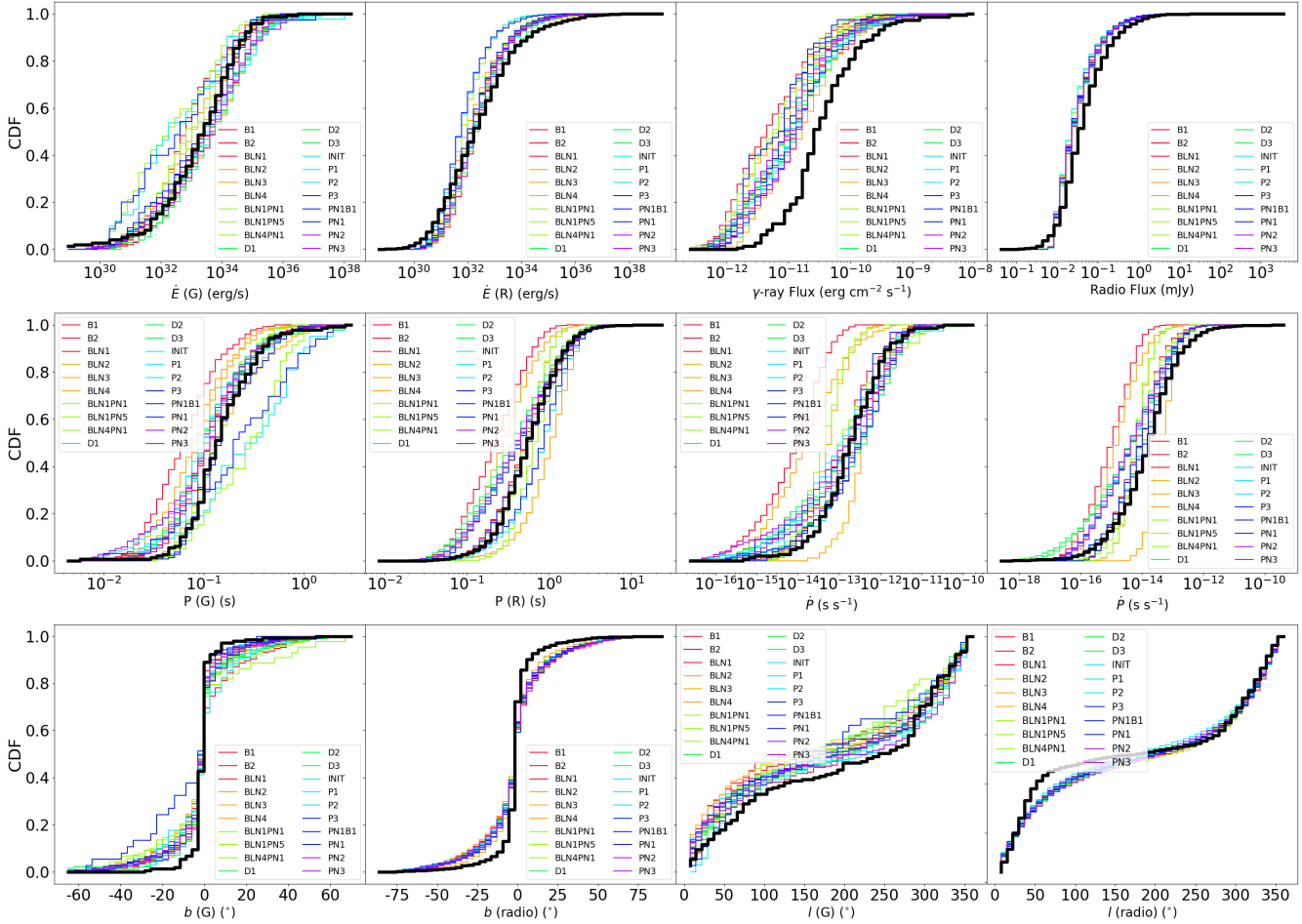


**Figure 2.** CDFs of physical quantities produced by the COMPAS models described in Table 1 (coloured), compared to the data from the catalogs (black). CDFs from a given model are drawn from a randomised sampling from 10 realisations. From top left to bottom right, the panels show the distributions of  $\gamma$ -ray pulsar  $\dot{E}$ , radio pulsar  $\dot{E}$ ,  $\gamma$ -ray flux, radio flux,  $\gamma$ -ray pulsar period, radio pulsar period,  $\gamma$ -ray pulsar  $\dot{P}$ , radio pulsar  $\dot{P}$ ,  $\gamma$ -ray pulsar galactic latitude, radio pulsar galactic latitude,  $\gamma$ -ray pulsar galactic longitude and radio pulsar galactic longitude.

**Table 3.** Results of the simulations: number of different types of pulsars. Columns left to right: COMPAS model; pulsars that are detected in radio ( $N_R$ ); pulsars detected in  $\gamma$ -ray ( $N_G$ ); radio-quiet  $\gamma$ -ray loud pulsars ( $N_{RQGL}$ ); radio-loud  $\gamma$ -ray quiet pulsars ( $N_{RLGQ}$ ); radio-loud  $\gamma$ -ray pulsars ( $N_{RLGL}$ ). The first row lists the total number of pulsars in the radio and  $\gamma$ -ray catalogs (Manchester et al., 2005; Smith et al., 2023). MSPs are excluded as we focus on canonical pulsars. For the simulations, the values and uncertainties are obtained from the average and standard deviation of 10 different realisations of each model.

Model	$N_R$	$N_G$	$N_{RQGL}$	$N_{RLGQ}$	$N_{RLGL}$
Catalogs	2715	160	90	2645	70
INIT	3414 $\pm$ 46	195 $\pm$ 13	113 $\pm$ 6	3331 $\pm$ 47	82 $\pm$ 10
D1	3412 $\pm$ 55	188 $\pm$ 7	103 $\pm$ 8	3327 $\pm$ 53	85 $\pm$ 7
D2	2533 $\pm$ 25	208 $\pm$ 8	127 $\pm$ 6	2451 $\pm$ 29	81 $\pm$ 9
D3	3357 $\pm$ 40	194 $\pm$ 6	114 $\pm$ 6	3277 $\pm$ 40	80 $\pm$ 7
B1	2803 $\pm$ 56	185 $\pm$ 10	108 $\pm$ 4	2726 $\pm$ 57	77 $\pm$ 8
B2	20466 $\pm$ 89	612 $\pm$ 18	199 $\pm$ 7	20053 $\pm$ 87	413 $\pm$ 14
P1	1953 $\pm$ 34	41 $\pm$ 4	22 $\pm$ 2	1935 $\pm$ 35	18 $\pm$ 2
P2	3366 $\pm$ 45	210 $\pm$ 10	112 $\pm$ 5	3269 $\pm$ 47	98 $\pm$ 8
P3	1993 $\pm$ 26	35 $\pm$ 4	18 $\pm$ 3	1976 $\pm$ 27	16 $\pm$ 3
PN1	3263 $\pm$ 47	138 $\pm$ 9	75 $\pm$ 4	3200 $\pm$ 45	62 $\pm$ 6
PN2	3436 $\pm$ 64	190 $\pm$ 9	109 $\pm$ 6	3356 $\pm$ 60	81 $\pm$ 7
PN3	3337 $\pm$ 59	188 $\pm$ 8	102 $\pm$ 7	3251 $\pm$ 53	87 $\pm$ 8
BLN1	3434 $\pm$ 58	184 $\pm$ 10	106 $\pm$ 7	3356 $\pm$ 58	78 $\pm$ 6
BLN2	12020 $\pm$ 93	451 $\pm$ 14	179 $\pm$ 12	11748 $\pm$ 93	272 $\pm$ 13
BLN3	1773 $\pm$ 28	185 $\pm$ 8	124 $\pm$ 7	1711 $\pm$ 26	62 $\pm$ 7
BLN4	7918 $\pm$ 74	373 $\pm$ 13	177 $\pm$ 7	7723 $\pm$ 70	196 $\pm$ 10
PN1-B1	2736 $\pm$ 27	146 $\pm$ 7	79 $\pm$ 5	2669 $\pm$ 26	67 $\pm$ 6
BLN1-PN1	3446 $\pm$ 59	152 $\pm$ 5	75 $\pm$ 4	3369 $\pm$ 59	77 $\pm$ 5
BLN1-PN5	2586 $\pm$ 34	52 $\pm$ 5	25 $\pm$ 3	2559 $\pm$ 33	27 $\pm$ 5
BLN4-PN1	7727 $\pm$ 79	262 $\pm$ 13	96 $\pm$ 4	7562 $\pm$ 80	166 $\pm$ 13

- In general, our models reproduce  $\gamma$ -ray pulsar populations that have a better resemblance to the catalog, compared to the modelled radio pulsar populations. This means that more physical quantities for  $\gamma$ -ray pulsars have p-values  $> 0.05$  compared to radio pulsars.
- The Galactic coordinates of the pulsar populations seem to be better fitted compared to the other physical quantities. This seems to confirm that the Galactic model, kick distribution and other related models used in this work is good enough. However, the large distance uncertainties of the pulsars in the catalog might be a restraint on this modelling.

Since none of the COMPAS models produce results that completely agree with observations, we will not attempt to choose a best-fit model. Here we examine and discuss a few models that perform better than the rest by checking the number of quantities that have p-value  $> 0.05$ . The PN1-B1, P2, and INIT models have 7 quantities with large p-values; and the P1, PN1 and D3 models have 6 quantities with large p-values. We examine these models in detail below, combining the results from Table 3 in the discussion. In addition, we also pay attention to the B1 and BLN1-PN4 models, as discussed below. From Table 4, it is obvious that some models are badly matched to the observations, including the D2, B2, P1, P3, PN1, BLN2, BLN3, BLN4, BLN1-PN1, and BLN4-PN4. The bad match for model D2 means that short magnetic decay timescale is not favoured. The bad match for models B2, BLN2, BLN3, and

BLN4, means that low birth magnetic field is not favored. The bad match for models P1, P3 and PN1 means that large birth rotational periods are not favoured. On the other hand, simply by examining this table, it appears that the model's INIT, D1, D3, B1, P2, BLN1, and PN1-B1 match the catalogs. Combining the results in Tables 4 and 5, it appears that models INIT, D3, PN1-B1 can best describe the observed properties of canonical pulsar populations. Examining the CDFs on the physical parameters of all 10 realisations of the INIT, D3, and PN1-B1 models, it appears that visually, the realisations of the PN1-B1 model best match to the distributions of the physical parameters out of the three models.

Overall, as discussed above, we determine that the PN1-B1 model best describes the pulsar initial conditions which produce pulsar populations in agreement with the catalogs. We first plot the CDFs of the quantities listed in Table 5 for PN1-B1 model in Fig. 3, showing the results of all 10 realisations. Overall, the CDFs of a given physical quantity between the model and the catalog match well with each other. We then visualise the results with the  $P-\dot{P}$  diagrams of the  $\gamma$ -ray pulsars and radio pulsars generated from one randomly chosen realisation of the PN1-B1 model, and overlay them with the canonical pulsars from the catalog, as shown in Fig. 4. These diagrams, for pulsar researchers, would serve as a better illustration for the comparison between the model and the catalog. It is obvious that for the  $\gamma$ -ray pulsars, the simulation and catalog pulsar populations occupy the same part of the

**Table 4.** Percentage difference (PD) between the numbers of different types of pulsars generated in COMPAS models and the radio and  $\gamma$ -ray catalogs. For all the models, except for B1 and PN1-B1, the comparisons are carried out after scaling the number of radio pulsars to be the same as the catalog. First five columns: percent differences of the numbers of radio,  $\gamma$ -ray, radio-quiet  $\gamma$ -ray-loud, radio-loud  $\gamma$ -ray-quiet, and radio-loud  $\gamma$ -ray-loud pulsars between each model and the catalogs. Sixth column: percent difference of the ratio between radio and  $\gamma$ -ray pulsars between each model and the catalogs. Seventh column: percent difference of the ratio between radio and  $\gamma$ -ray pulsars between each model and the catalogs. Last column: star formation rate of each model after scaling by the number of radio pulsars.

Model	PD <sub>R</sub>	PD <sub>G</sub>	PD <sub>RQGL</sub>	PD <sub>RLGQ</sub>	PD <sub>RLGL</sub>	PD <sub>Q1</sub>	PD <sub>Q2</sub>	SFR ( $M_{\odot}/\text{yr}$ )
INIT	-	3.1%	0.0%	0.11%	7.14%	7.01%	1.2%	0.95
D1	-	6.25%	8.9%	3.97%	2.8%	6.95%	5.5%	0.95
D2	-	39.4%	51.1%	0.68%	24.3%	28.2%	22.6%	1.3
D3	-	1.9%	2.2%	0.2%	7.1%	1.9%	11.3%	0.97
B1*	3.24%	15.6%	20%	3.1%	10%	10.72%	9.37%	1.2
B2	-	49.3%	71.1%	0.6%	21.4%	97%	62.3%	0.16
P1	-	64.4%	65.6%	1.7%	64.3%	180.5%	4.7%	1.67
P2	-	5.6%	0.0%	0.3%	12.8	5.6%	11%	0.97
P3	-	70%	72.2%	1.7%	68.6%	235.3%	12.5%	1.6
PN1	-	28%	31%	0.64%	27%	39.30%	5.47%	1.0
PN2	-	6.9%	5%	0.26%	9.3%	6.54%	4.69%	0.95
PN3	-	5%	7.8%	0.0%	1.4%	4.6%	8.6%	0.98
BLN1	-	9.4%	6.7%	0.3%	11.4%	9.9%	6.2%	0.95
BLN2	-	36.9%	55.5%	0.3%	12.8%	57%	56.2%	0.27
BLN3	-	76.9%	111.1%	0.9%	35.7%	43.5%	56.2%	1.84
BLN4	-	20%	32.2%	0.1%	3.4%	24.9%	29.7%	0.41
PN1-B1*	0.7%	8.75%	12.2%	0.9%	4.3%	10.4%	7.8%	1.2
BLN1-PN1	-	25%	34.4%	0.3%	12.8%	33.6%	24.2%	0.94
BLN1-PN5	-	65.6%	71.1%	1.5%	60%	193%	28.1%	1.26
BLN4-PN1	-	42.5%	62.2%	0.03%	17.1%	73.8%	54.7%	0.42

\* models not scaled.



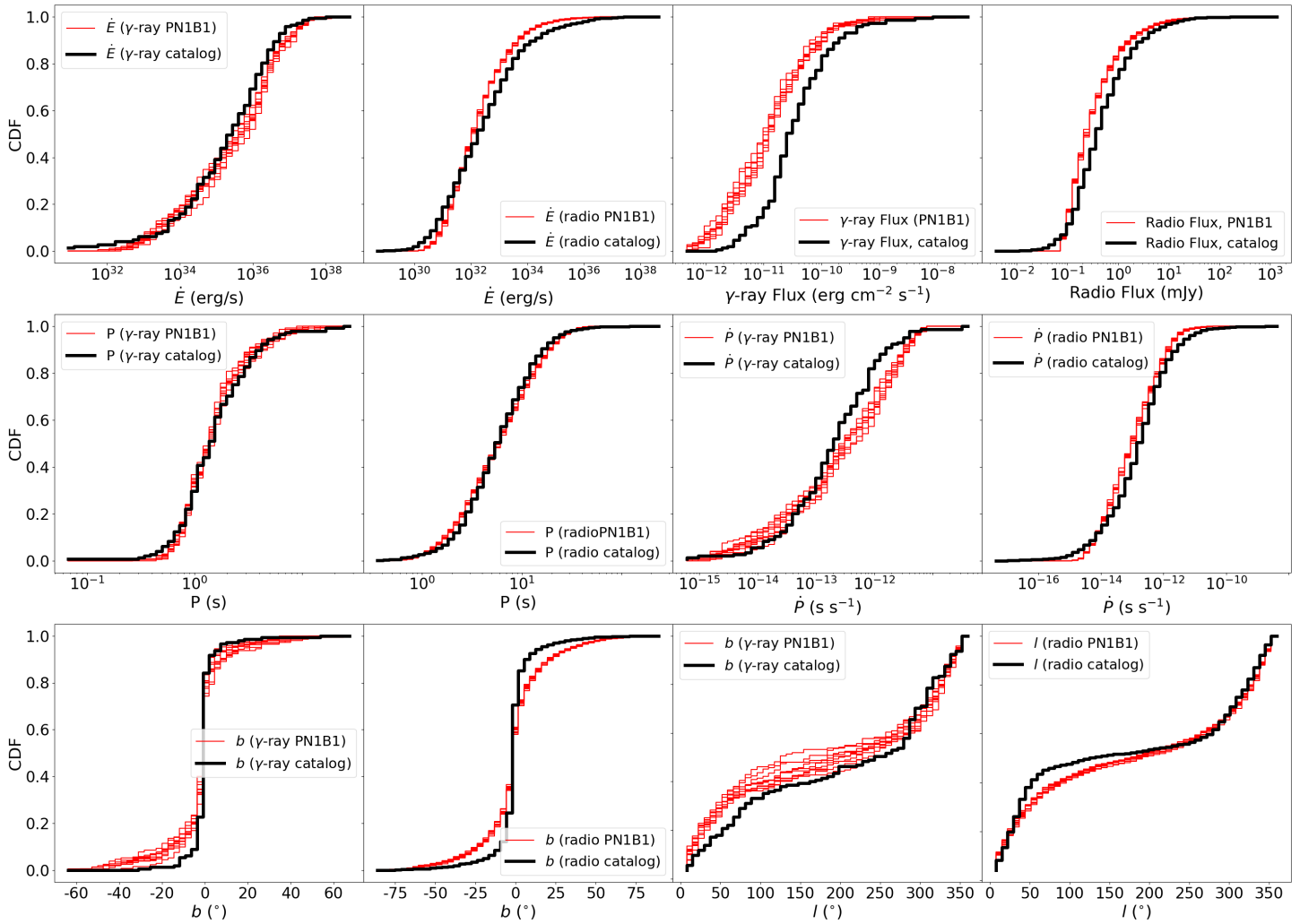


**Figure 3.** CDFs of various physical quantities predicted/produced by the PN1-B1 model (red), compared to the data from the catalogs (blue). The red lines in these plots are from all ten realisations of the PN1B1 model that are sampled randomly as described in § 2.9. From top left to bottom right, the panels show the distributions of  $\gamma$ -ray pulsar  $\dot{E}$ , radio pulsar  $\dot{E}$ ,  $\gamma$ -ray flux, radio flux,  $\gamma$ -ray pulsar period, radio pulsar period,  $\gamma$ -ray pulsar  $\dot{P}$ , radio pulsar  $\dot{P}$ ,  $\gamma$ -ray pulsar galactic latitude, radio pulsar galactic latitude,  $\gamma$ -ray pulsar galactic longitude and radio pulsar galactic longitude.

**Table 5.** P-value of Mann-Whitney U Test, comparing the physical quantities obtained from simulations and catalog. Quantities listed in the second to the third last columns are, respectively, radio flux,  $\gamma$ -ray flux, period of radio pulsars, period of  $\gamma$ -ray pulsars,  $\dot{P}$  of radio pulsars,  $\dot{P}$  of  $\gamma$ -ray pulsars,  $\dot{E}$  of radio pulsars,  $\dot{E}$  of  $\gamma$ -ray pulsars, Galactic latitude of radio pulsars, Galactic latitude of  $\gamma$ -ray pulsars, Galactic longitude of radio pulsars, and Galactic longitude of  $\gamma$ -ray pulsars. The last column is the number of the quantities that have p-values  $> 0.05$  for each model. For a given model, the p-values for each parameter is determined using the random realisation of the model that is shown in Fig. 2

Model	$\dot{E}(G)$	$\dot{E}(R)$	Flux(G)	Flux(R)	Period(G)	Period(R)	$\dot{P}(G)$	$\dot{P}(R)$	b(G)	b(R)	l(G)	l(R)	NO
INIT	0.059	0.09	0.0	0.0	0.001	0.0	0.999	0.0	0.767	0.487	0.144	0.052	7
D1	0.58	0.526	0.0	0.0	0.0	0.0	0.443	0.0	0.085	0.541	0.048	0.011	5
D2	0.0	0.0	0.0	0.0	0.001	0.0	0.05	0.0	0.548	0.728	0.426	0.017	4
D3	0.113	0.528	0.0	0.0	0.003	0.0	0.644	0.0	0.461	0.085	0.112	0.047	6
B1	0.019	0.094	0.0	0.0	0.003	0.4	0.266	0.0	0.117	0.579	0.041	0.006	5
B2	0.0	0.0	0.0	0.0	0.0	0.0	0.0	0.0	0.845	0.572	0.058	0.064	4
P1	0.524	0.0	0.0	0.0	0.161	0.0	0.497	0.0	0.819	0.515	0.988	0.003	6
P2	0.758	0.363	0.0	0.0	0.0	0.0	0.241	0.0	0.242	0.893	0.388	0.073	7
P3	0.097	0.0	0.0	0.0	0.029	0.0	0.646	0.0	0.04	0.405	0.003	0.124	4
PN1	0.379	0.003	0.0	0.0	0.66	0.0	0.181	0.0	0.405	0.074	0.267	0.013	6
PN2	0.312	0.09	0.0	0.0	0.006	0.0	0.295	0.0	0.315	0.589	0.019	0.008	5
PN3	0.193	0.858	0.0	0.0	0.008	0.0	0.031	0.0	0.159	0.265	0.624	0.031	5
BLN1	0.191	0.022	0.0	0.0	0.007	0.005	0.048	0.0	0.868	0.047	0.53	0.084	4
BLN2	0.038	0.042	0.0	0.0	0.0	0.0	0.0	0.0	0.268	0.035	0.014	0.005	1
BLN3	0.006	0.0	0.0	0.0	0.908	0.0	0.0	0.0	0.292	0.876	0.121	0.107	5
BLN4	0.84	0.029	0.0	0.0	0.0	0.0	0.0	0.0	0.535	0.159	0.102	0.019	4
PN1-B1	0.618	0.004	0.0	0.0	0.687	0.266	0.065	0.0	0.296	0.836	0.189	0.007	7
BLN1-PN1	0.626	0.002	0.0	0.0	0.54	0.001	0.017	0.0	0.476	0.109	0.151	0.034	5
BLN1-PN5	0.0	0.0	0.0	0.0	0.0	0.0	0.759	0.0	0.654	0.178	0.283	0.001	4
BLN4-PN1	0.0	0.002	0.0	0.0	0.102	0.0	0.0	0.0	0.224	0.086	0.031	0.02	3

parameter space. For the radio pulsar populations, however, the shapes are slightly different between the catalog and simulation. There are fewer radio pulsars from the simulation that occupy the top left corner of the  $P$ - $\dot{P}$  diagram, indicating that the simulation produces fewer young, more energetic pulsars with higher  $\dot{E}$ . There are more radio pulsars from the simulation that occupy the parameter space in the bottom left part of the plot, indicating there are more pulsars with lower magnetic field strength compared to the catalog.

In Smith *et al.* (2019), a discussion of distance biases on the pulsar catalog was presented. Lower  $\dot{E}$  pulsars, the majority of which are off the Galactic plane, cannot be detected easily due to their low efficiency, small sample, and possible large distance. However, Smith *et al.* (2019) suggest that if low  $\dot{E}$  pulsars emit in  $\gamma$ -rays, it would be useful to use the population synthesis approach to help understand if a large population of such pulsars would contribute to a part of the diffuse Galactic  $\gamma$ -ray emission. This work does not provide a full population modelling of pulsars, especially old pulsars, as only the recent star formation history is considered. Therefore we are unable to determine if the diffuse background can be attributed to old pulsars. This will be discussed in a follow-up study.

Here we show the heuristic flux of detected and stacked pulsars in Fig. 5, as for the detected pulsars, both those from the simulation and the Fermi-LAT catalog occupy similar parts of the parameter space. The heuristic flux is defined as  $\sqrt{\dot{E}/4\pi d^2}$ , and is often used in observation to estimate the po-

tential  $\gamma$ -ray flux of a pulsar, especially if it is not detectable. In Fig. 5, excluding those with estimated distance 25 kpc (which is the flagged value based on the dispersion measure (Yao *et al.*, 2017)), the stacked pulsars from the simulation, in general, have larger distances compared to those from the catalog. This might also stem from the fact that the distance measurements of the stacked pulsars from the catalog are largely uncertain.

We show the spatial coordinates of detected pulsars in Figs. 6 & 7. These plots show a similar story as the  $P$ - $\dot{P}$  diagram, where the distributions of  $\gamma$ -ray pulsars across the Galaxy seem to agree better with the catalogs, and the radio pulsars less so. We note the main difference in the spatial distribution of radio pulsars between the catalog and simulation is a large population of radio pulsars around the Galactic Centre is present in the simulation. There is however no such population present in the catalog. There are two possible causes for this issue: 1). The underlying stellar population that produced the pulsars is extremely concentrated around the Galactic Centre, making it the dominant effect. It is reasonable for this to happen, even with the selection effect accounting for high sky temperature around this direction of observation. 2). It is also likely that the distance measurements of the detected radio pulsars are largely uncertain, especially towards the direction of the Galactic Centre, due to high DM/scatter in this direction, causing the catalog pulsars to have inaccurate coordinates.

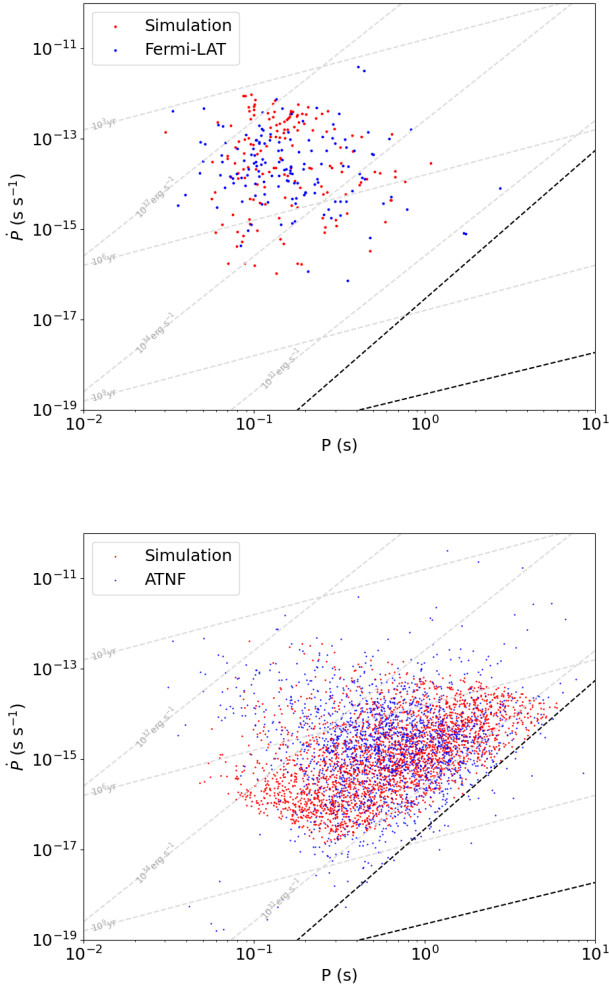


**Figure 4.** Top:  $P-\dot{P}$  diagram of *Fermi* detected canonical pulsars (blue) and detected  $\gamma$ -ray pulsars from the characteristic PN1-B1 model (red); bottom:  $P-\dot{P}$  diagram of radio detected canonical pulsars as recorded in the ATNF catalog (blue) and detected radio pulsars from the characteristic PN1-B1 model (red). The two black dashed lines represent the death-lines described in Eqs. 6 & 7. The gray dashed lines labeled  $10^3$  yr,  $10^6$  yr, and  $10^9$  yr represent constant characteristic age each respectively; and those labeled with  $10^{31}$  erg  $s^{-1}$ ,  $10^{33}$  erg  $s^{-1}$ , and  $10^{37}$  erg  $s^{-1}$  represent constant  $\dot{E}$  each respectively.

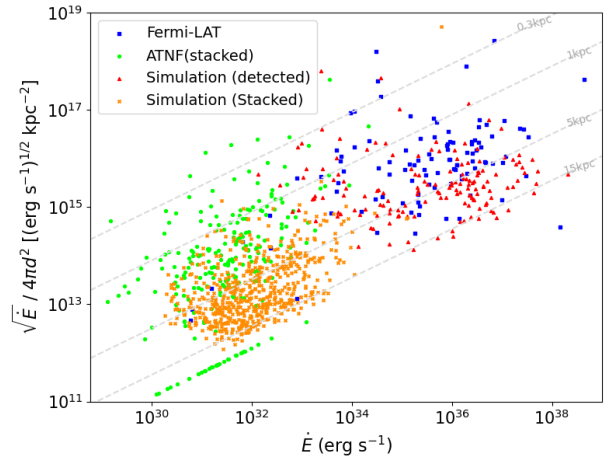


**Figure 5.** Expected  $\gamma$ -ray flux of pulsars (the heuristic flux) as a function of the spindown luminosity  $\dot{E}$  (similar to Fig. 7 in [Smith et al., 2019](#)). We plot the expected  $\gamma$ -ray flux of pulsars (the heuristic flux) when assuming  $L_\gamma = \sqrt{10^{33} \dot{E}} \text{ erg s}^{-1}$ . Blue squares are *Fermi*-LAT detected pulsars, red triangles are the detected pulsars from the simulation using the PN1-B1 model, green dots are the pulsars from the sample list of [Song et al. \(2023\)](#), and the orange crosses are the pulsars that satisfy the criteria of being stacked from the simulation using the PN1-B1 model. The gray dotted lines labelled 0.3 kpc, 1 kpc, 5 kpc and 15 kpc represent those of constant distance respectively. Most of the pulsars stacked in [Song et al. \(2023\)](#) with  $\dot{E} < 10^{33} \text{ erg s}^{-1}$  remain undetected in spite of having similar heuristic fluxes to those detected with higher  $\dot{E}$ . Most of the pulsars being stacked from the simulation have larger distances compared to those from [Song et al. \(2023\)](#).

### 3.3 Impact of $\gamma$ -ray Luminosity Model and Sensitivity

We understand that there are impacts on this work from various model choices implemented in this study. Here we discuss the impact on the simulation results from two model choices:  $\gamma$ -ray luminosity of pulsars, and the  $\gamma$ -ray sensitivity limit.

Luminosity determination can impact the simulation results from the uncertainty in the fitting of the fundamental plane itself. As described above in § 2.8, we use the fundamental plane relations with the best-fit parameters without any scatter. Introducing the uncertainties back into the parameters would end up with slightly different fundamental plane relations for each pulsar. We attempt to set the fundamental plane with the uncertainties included in Eq. 17, and re-analyse the PN1-B1 model.

In Fig. 8, we plot the  $\gamma$ -ray luminosity of the observed pulsars in PN1-B1 model and catalog vs. their  $\dot{E}$  for both the original analysis and the  $\gamma$ -ray luminosity with the scattered fundamental plane. Overall, when taking the fundamental plane without any uncertainties, the *Fermi* detected pulsars and pulsars from the simulation follow the fundamental plane relationship. The obvious effect of using a scattered fundamental plane is that the luminosity in the model does not follow the apparent fundamental plane relations where  $L \sim \dot{E}^{0.39}$ . As shown in the right panel of the figure, the correlation is closer to the  $L \sim \dot{E}$  line. This is simply due to the fact that the scatter from the power law indices on various quantities have uncertainties that are too big, causing this up scatter. Addi-

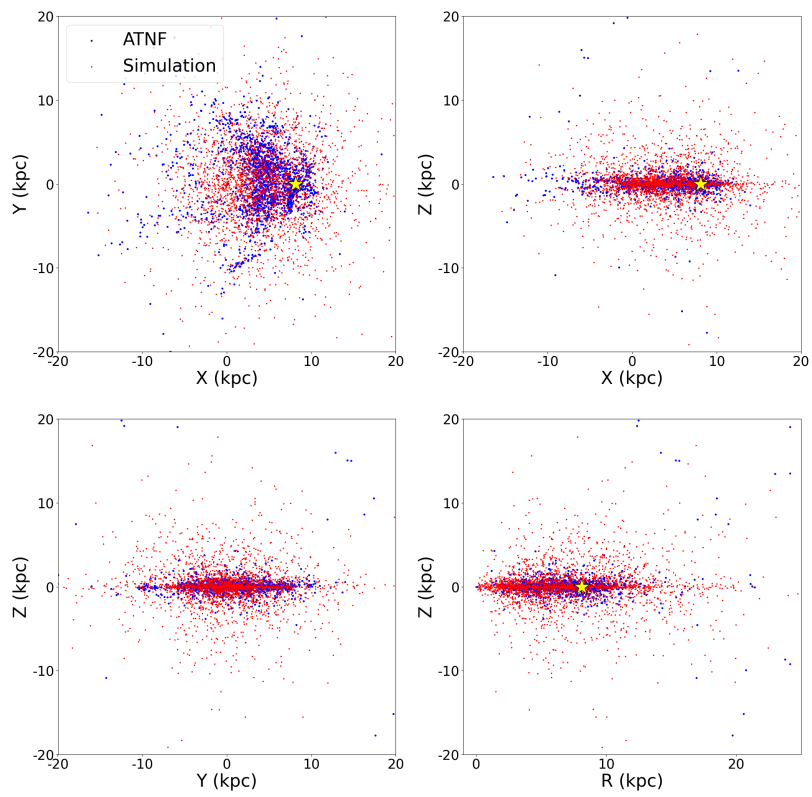


**Figure 6.** Galactocentric coordinates of radio pulsars from the catalog (blue) and from PN1-B1 model (red). The yellow star in all panels except for the Y-Z planes indicates the location of the Sun.



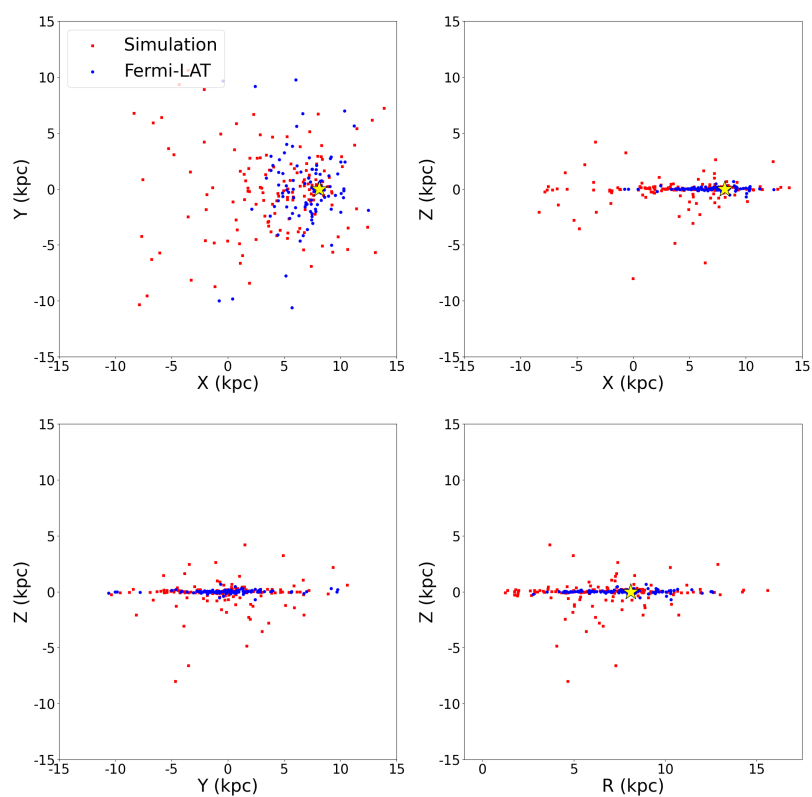


**Figure 7.** Galactocentric coordinates of  $\gamma$ -ray pulsars from the catalog (blue) and from PN1-B1 model (red). The yellow star in all panels except for the Y-Z planes indicates the location of the Sun.

tionally, some pulsars have luminosity larger than their  $\dot{E}$  both in simulation and catalog. When this occurs in the simulation, it is due to the observational effect of the flux correction factor which is caused by the beaming of the pulsar. There are other reasons for this to happen in observed pulsars, most likely due to the large errors in the estimation of pulsar distances and beaming geometry of the pulsars.

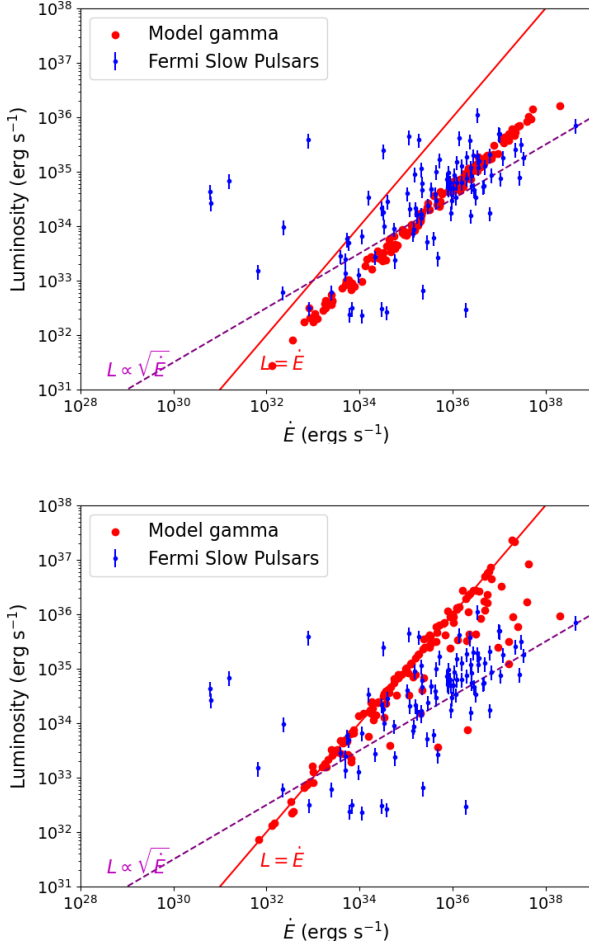


**Figure 8.** Left:  $\gamma$ -ray luminosity of all detected pulsars vs.  $\dot{E}$ , assuming for fixed fundamental plane. Right:  $\gamma$ -ray luminosity of all detected pulsars vs. their  $\dot{E}$  for the scattered fundamental plane. In both panels, the blue data points with error bars are the pulsars detected by Fermi-LAT and the red data points are from the simulation using PN1-B1 model. The magenta dashed line represents the heuristic relation  $L_\gamma = \sqrt{10^{33}\dot{E}}$  and the red solid line represents the limit of energy conservation as  $L_\gamma = \dot{E}$ .

We also discovered that the choice of the sensitivity limit for the radio-detected pulsars, as described in § 2.8.2, can impact the final results. Specifically, when we change our assumption about the sensitivity floor, the detected population in the model will change too. As stated in § 2.8.2, we deviate from the standard 4FGL sensitivity based on the radio detectability of the pulsar. We define  $\alpha$  as the factor to raise the sensitivity floor from the default 4FGL-DR4 sensitivity when the pulsar is not detected in the radio; and  $\beta$  as the factor to lower the sensitivity floor when the pulsar is detected in the

radio. Here we set a few different options for the combination of  $\alpha$  and  $\beta$  as described in Table. 6, then re-run the analysis pipelines. We compare the results by checking the number of  $\gamma$ -ray pulsars produced in each instance, as well as the ratio between radio-quiet and radio-loud  $\gamma$ -ray pulsars ( $q$ ). This analysis is performed on the PN1-B1 model with 6 different combinations of  $\alpha$  and  $\beta$ . Table. 6 shows the results of the number of  $\gamma$ -ray pulsars detected in the model ( $N_G$ ) as well as the ratio  $q$  between the  $\gamma$ -ray loud and  $\gamma$ -ray quiet radio pulsars. When  $\alpha$  increases, more  $\gamma$ -ray pulsars are detected and the ratio between radio-quiet and radio-loud  $\gamma$ -ray pulsars increases. In this case, most of the increase of  $N_G$  can be attributed to more radio-quiet pulsars being detected in  $\gamma$ -rays. When  $\beta$  increases, more  $\gamma$ -ray pulsars are detected and the ratio between radio-quiet and radio-loud  $\gamma$ -ray pulsars decreases. In this case, most of the increase of  $N_G$  can be attributed to more radio pulsars being detected in  $\gamma$ -rays.

**Table 6.** Results of different setup for the  $\gamma$ -ray sensitivity.  $\alpha$  is the factor to raise the sensitivity floor from the 4FGL value at the location if the pulsar is not detected in radio, and  $\beta$  is the factor to lower the sensitivity from the 4FGL value at the location if the pulsar is detected in radio. Model-0 is the same that adopted for the results above. Models 1-6 are additional models.  $N_G$  is the number of  $\gamma$ -ray pulsars produced by the model given the sensitivity setup, and the  $q$  is the ratio between the radio-quiet and radio-loud  $\gamma$ -ray pulsars. Cat denotes the observed values for  $N_G$  and  $q$ .

Model	$\alpha$	$\beta$	$N_G$	$q$
Cat	–	–	160	90:70
0	1.5	5.0	152	87:65
1	1.0	3.0	171	122:49
3	1.0	5.0	171	114:57
3	1.25	4.0	160	99:61
4	2.0	1.0	81	62:19
5	2.0	2.5	98	57:41
6	2.0	4.0	128	68:60

Overall, this further confirms that there are multiple factors that impact the results of this study. Future development in better physical understanding of pulsar emission mechanism and stronger correlation between the radio and  $\gamma$ -ray detection limit from the current population can further improve these results.

### 3.4 Low $\dot{E}$ Pulsars in $\gamma$ -rays

Theoretical studies of  $\gamma$ -ray emission from pulsars, such as the equatorial current sheet model (Pétri, 2012; Kalapotharakos et al., 2018; Hakobyan et al., 2023) or the outer gap model (Cheng et al., 1986a,b; Romani, 1996; Takata et al., 2011), seem to indicate that pulsars with  $\dot{E} < 10^{33}$  erg/s do not emit in  $\gamma$ -ray s. Indeed, if we investigate Eq. 17, it shows that at  $\dot{E} = 10^{33}$  erg/s, the  $\gamma$ -ray luminosity of a pulsar is equal to  $\dot{E}$ , reaching maximum efficiency. With  $\dot{E} < 10^{33}$ , if we still follow the fundamental plane relation, the  $\gamma$ -ray luminosity of the pulsar becomes larger than  $\dot{E}$ , breaking the conservation of energy. It is also worth noting that according to Kalapotharakos et al. (2019, 2022), the fundamental plane relations are rooted in the

equatorial current sheets model with theoretical foundations.

However, the most up-to-date 4FGL/3PC catalogs include a handful of  $\gamma$ -ray pulsars that are detected with  $\dot{E} < 10^{33}$  erg/s. Given the low number of detections of  $\gamma$ -ray pulsars with  $\dot{E} < 10^{33}$  erg/s, there is no clear understanding of their emission mechanism. In fact, according to Song et al. (2023), pulsars might have a universal, weak, and isotropic  $\gamma$ -ray emission. We try to replicate the stacking analysis performed in Song et al. (2023) to show further evidence of the possible emission mechanism for low  $\dot{E}$  pulsars.

We choose pulsars from the PN1-B1 model that are radio loud,  $\gamma$ -ray quiet that are at least  $20^\circ$  away from the Galactic plane for this study, consistent with Song et al. (2023). There are 590 such pulsars in the simulation. We then assign each pulsar with two different  $\gamma$ -ray luminosities, one that follows the fundamental plane if  $\dot{E} > 10^{33}$  erg s $^{-1}$  and  $L = 0.8\dot{E}$  when  $\dot{E} < 10^{33}$  erg s $^{-1}$ ; and the other one is assigned a luminosity drawn from a log normal distribution  $\log_{10} \sim N(32, 0.5)$  (ergs/s). The former luminosity assignment corresponds to beamed  $\gamma$ -ray emission correlated to the  $\dot{E}$  of each pulsar, and the latter corresponds to the universal, weak and isotropic  $\gamma$ -ray emission. For the first emission mechanism, we still account for the  $\gamma$ -ray beaming effect discussed in § 2.8.3 when being stacked, while the isotropic emission does not need to be beamed.

We then calculate the average luminosity of the pulsars in five different  $\dot{E}$  bins, with each bin having the same number of pulsars. We check these results in a similar way to Fig. 6 in Song et al. (2023). Here in this work, we choose the canonical pulsars from Song et al. (2023) and plot them in Fig. 9, and use this as the observational results to be compared with the model. We then plot in Fig. 9 the average luminosity vs.  $\dot{E}$  from the model with three different scenarios: only the fundamental plane is considered, only isotropic emission is considered, and combining both. Unfortunately, because the observational results are largely uncertain at this point, we are unable to determine which would be a better fit to describe the emission mechanism of lower  $\dot{E}$  pulsars. We either need a better understanding of pulsar emission in this regime, or more data to improve the observational results.

Another way to examine the results and potential emission mechanism is to compare the spectral energy distributions (SEDs) for various scenarios. We calculate the stacked SED of the 590 pulsars for the fundamental plane emission and isotropic emission as described above. The  $\gamma$ -ray spectral parameters of the pulsars,  $E_{\text{cut}}$  and PL index before cutoff, are drawn from the described text above. When considering the fundamental plane emission, a pulsar needs to be beamed towards the observer. When considering the isotropic emission, it does not need to be beamed. Averaging the SEDs, we can produce the stacked SEDs for both scenarios as shown in Fig. 10. We compare this result to Song et al. (2023) as well as the averaged pulsar SED from McCann (2015). As expected, if considering the FP emission, this stacked pulsar population is relatively older compared to the young, energetic pulsars, hence it is somewhere in between the averaged young pulsar

and MSP SED. That does mean that this is much more luminous than the stacked pulsars from Song et al. (2023). When considering the isotropic emission, however, the SED is much less luminous compared to the stacked pulsars from the data. Neither of our models here can completely explain the observation. It might be a mixture of both scenarios that can account for the observation, averaging out to the observed data points.

Many low  $\dot{E}$  pulsars are located outside of the Galactic plane (Smith et al., 2023). It is commonly believed that the high latitude pulsars are a result of pulsars receiving larger kicks when they went through supernova explosions. The results from this work can be used to confirm if that is indeed the case, as the kick velocities are one of the modelled components in our population synthesis models. In Fig. 11, we show the distributions of kick velocities received by pulsars from the model that are either detected or stacked, as selected above. Consistent with our hypothesis, we find that the high latitude, low  $\dot{E}$  pulsars in the stacked sample received larger natal kicks than the typical detected population.

#### 4. Future Development

As the first of a series of studies using COMPAS to study  $\gamma$ -ray pulsar populations, there are some caveats as discussed above, and these are summarised below:

1. This work currently does not include MSP populations. Pulsar recycling physics will be implemented in a direct follow-up of this work so that a full population study of pulsars including MSPs can be carried out. MSPs are products of binary evolution, and so comparing to binary evolution models will be important to fully understand the population.
2. Some NSs are formed through accretion-induced collapses, and these NSs are not accounted for in this work. This is mainly because it takes much longer than 200 Myrs for a NS to form through this channel, and they are naturally left out from this study as we only choose to include binary systems formed within the most recent 200 Myrs. Additionally, neutron stars formed through accretion-induced collapse may directly form MSPs (e.g., Hurley et al., 2010; Tauris et al., 2013; Ruiter et al., 2019), which are not the focus of this work.
3. We currently lack a physical model for the birth spin periods and magnetic fields for pulsars as a function of the progenitor properties (cf. Mandel & Müller, 2020, for neutron star masses and kicks). This work, and any follow-up in the foreseeable future will only be able to use some empirically assumed distribution of these quantities.
4. We have neglected the population of magnetars with long spin periods and high magnetic fields (e.g., Popov et al., 2010; Gullón et al., 2015; Makarenko et al., 2021). As with canonical pulsars, most magnetars are isolated, whilst their massive star progenitors were presumably born in binaries. Binary interactions such as stellar mergers may be responsible for producing highly magnetic neutron stars (Schneider et al., 2019).

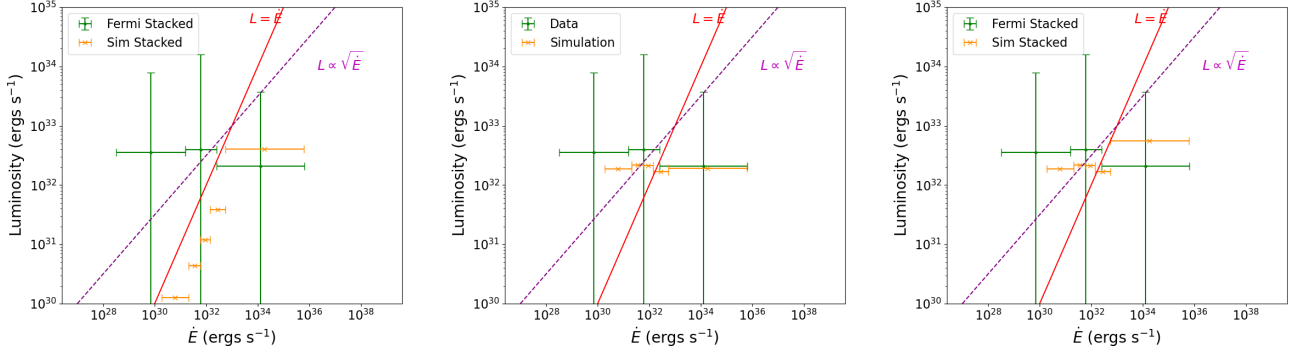


**Figure 9.** Left:  $\gamma$ -ray luminosity vs.  $\dot{E}$  for stacked pulsars. The green data points with error bars in both directions are from Song *et al.* (2023) and the orange data points with only horizontal error bars are from the simulation using PN1-B1 model. The magenta dashed line represents the heuristic relation  $L_\gamma = \sqrt{10^{33}\dot{E}}$  and the red solid line represents the limit of energy conservation as  $L_\gamma = \dot{E}$ . The left panel calculates the stacked luminosity from the simulation by assuming the stacked pulsars have a luminosity that follows the fundamental plane while  $\dot{E} > 10^{33} \text{ erg s}^{-1}$  and  $L_\gamma = 0.8\dot{E}$  when  $\dot{E} < 10^{33} \text{ erg s}^{-1}$ . The middle panel is calculating the luminosity assuming all these pulsars have a weak, isotropic  $\gamma$ -ray emission follows a log-normal distribution where  $\log L_\gamma \sim N(32, 0.5)$ . The right panel combines both.

After addressing the above-mentioned caveats, we would be able to simulate full populations of NSs and broaden the scope of our research with several different follow-up studies:

1. A full scope of pulsar population synthesis can enable the study of NS contribution to the diffuse  $\gamma$ -ray background (Fermi-LAT Collaboration, 2017)
2. The inclusion of MSPs in the population synthesis models would provide further insight into the possible MSP origin of the Galactic Centre GeV Excess (Hooper & Mohlabeng, 2016; Ploeg *et al.*, 2017; Eckner *et al.*, 2018).
3. A comparison of pulsar populations between the Galactic field and globular clusters with results from dynamical simulations, such as those from NBODY and CMC (e.g., Ye *et al.*, 2019, 2024).
4. After adding in the formation of MSPs and NSs formed through accretion-induced collapse, the model will be able to perform on the Hubble time scale. This will enable the modelling of merger events for gravitational wave detections, such as black hole-NS binaries (Chattopadhyay *et al.*, 2021), double NSs (Chattopadhyay *et al.*, 2020) and NS-white dwarf binaries.
5. Include magnetar physics in future versions of COMPAS and synthesize magnetar populations.
6. Investigate more sophisticated model comparison methods to fully explore the parameter space and identify a best-fit model that produces the population of pulsars observed to date. Several approaches have been taken in the literature, including hierarchical Bayesian parameter estimation (e.g., Ploeg *et al.*, 2020) and machine learning approaches (e.g., Ronchi *et al.*, 2021; Graber *et al.*, 2023). At present, such a large parameter space exploration is computationally infeasible using COMPAS. In a follow-up study, we will optimise, parameterise and automate our COMPAS simulations and post-processing pipelines so that the use of more sophisticated model exploration and comparison techniques becomes computationally feasible.

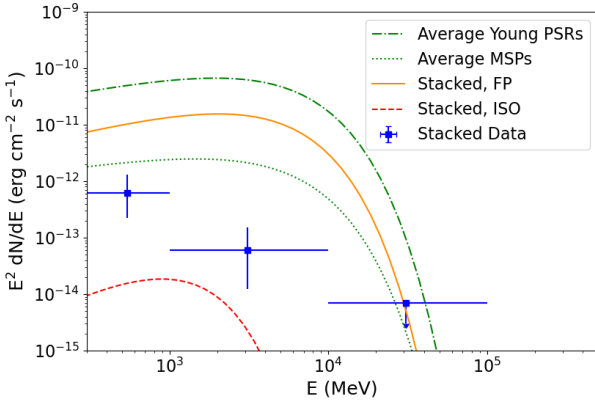


**Figure 10.** SED of stacked pulsars from the simulation using the PN1-B1 model. The orange solid curve is the averaged SED from the stacked pulsars in the simulation assuming they all follow the empirical fundamental plane (FP) emission mechanism in  $\gamma$ -rays, and the red dashed curve is for the same population of pulsars assuming they all emit weakly isotropic  $\gamma$ -ray emission (ISO). The blue data points with error bars are the averaged SED of the sampled canonical pulsars from Song *et al.* (2023), The green dotted-dashed curve represents the averaged SED of young pulsars, and the green dotted curve SED of MSPs (McCann, 2015).



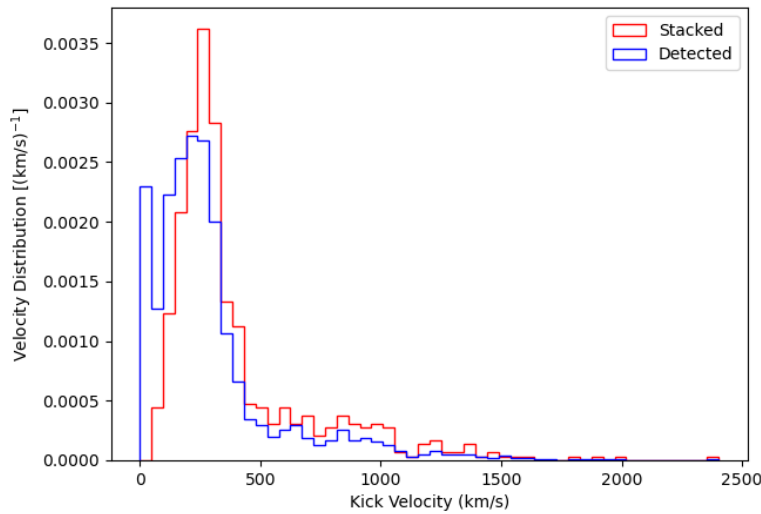


**Figure 11.** Kick distributions of simulated pulsars. The blue histogram shows the kick distribution of the pulsars detected in the simulation, and the red histogram shows the kick distribution of the stacked pulsars from the simulation. The selection of pulsars off of the Galactic plane preferentially selects pulsars born with large kick velocities.

In addition to varying the birth distributions of the pulsar properties (birth magnetic fields and spin periods), in future work, we aim to study how different binary properties, including initial orbital properties, different mass transfer theories, neutron star kick velocities and common envelope physics can impact the pulsar population, and how this population can be used to constrain the underlying physics of massive binary evolution.

## 5. Conclusions

We performed a population synthesis of the canonical Galactic pulsar population using the rapid binary population synthesis code COMPAS (Riley et al., 2022) on both radio and  $\gamma$ -ray canonical pulsars. We generated 20 different models for pulsar birth properties for COMPAS runs incorporating a magnetic braking model with a braking index of 3 for pulsar spindown. We discover that the PN1-B1 model, where the birth period of pulsar follows a normal distribution with  $\mu = 75$  ms and  $\sigma = 25$  ms, the birth magnetic field of pulsars follows a uniform distribution between  $10^{11}$  and  $10^{13}$  G, and magnetic decay time scale  $\tau_d = 500$  Myr best describes the observed pulsar population, based on the facts that:

1. PN1-B1 model produces the number of radio and  $\gamma$ -ray canonical pulsars that, given the star formation rate of the model, best fits the catalog.
2. The distribution of physical properties of radio and  $\gamma$ -ray pulsars produced from this model matches the catalog the best.

We then compare in detail the PN1-B1 model results to the catalog by examining the  $P-\dot{P}$  plots, the Galactocentric coordinates, and the heuristic flux between the simulation and the catalog. We also discussed the impact of the selection effect

on the population synthesis results, demonstrating that the slightest change in pulsar physics and observation sensitivity can bring significant differences to the final simulation.

Using the results from PN1-B1 model, we also attempted to explore the possible emission mechanism from low  $\dot{E}$  pulsars ( $\dot{E} < 10^{33}$  erg s $^{-1}$ ), and failed to make a distinction between a beamed emission mechanism or an isotropic emission mechanism.

We will follow up this study to include the Galactic MSP population and utilise the results to answer other physical questions, including the  $\gamma$ -ray diffuse background, Galactic Centre GeV excess, and gravitational wave events from a NS binary.

## Acknowledgement

The authors appreciate coding assistance from R. Wilcox and J. Riley, and helpful discussions from T. Paglione, J. Tan and J. Hurley.

**Funding Statement** This research was conducted by the Australian Research Council Centre of Excellence for Gravitational Wave Discovery (OzGrav), through project numbers CE170100004 and CE230100016. S. Stevenson is a recipient of an ARC Discovery Early Career Research Award (DE220100241). D. Chattopadhyay is supported by the UK's Science and Technology Facilities Council grant ST/V005618/1. This work used the OzSTAR high-performance computer at Swinburne University of Technology. OzSTAR is funded by Swinburne University of Technology and the National Collaborative Research Infrastructure Strategy (NCRIS).

**Competing Interests** None.

**Data Availability Statement** COMPAS is open source and hosted on Github. Due to the size of COMPAS output files, the authors can share configuration files used to produce the pop-synth results upon request.

Post-processing scripts will be hosted on Github as well. Before being made available on Github, they will be available upon request provided that this work is properly cited.

## References

- Abbott, B. P., Abbott, R., Abbott, T. D., et al. 2017, *Phys. Rev. Lett.*, 119, 161101
- Abdo, A. A., et al. 2008, *Science*, 322, 1218
- Abdo, A. A., Ackermann, M., Ajello, M., et al. 2009, *Science*, 325, 840
- Abdo, A. A., et al. 2013, *Astrophys. J. Suppl.*, 208, 17
- Asplund, M., Grevesse, N., Sauval, A. J., & Scott, P. 2009, *ARA&A*, 47, 481
- Bailyn, C. D., & Grindlay, J. E. 1990, *ApJ*, 353, 159
- Bates, S. D., Lorimer, D. R., Rane, A., & Swiggum, J. 2014, *Monthly Notices of the Royal Astronomical Society*, 439, 2893
- Bertsch, D. L., Brazier, K. T. S., Fichtel, C. E., et al. 1992, *Nature*, 357, 306
- Bradt, H., Rappaport, S., & Mayer, W. 1969, *Nature*, 222, 728
- Burgay, M., D’Amico, N., Possenti, A., et al. 2003, *Nature*, 426, 531
- Chattopadhyay, D., Stevenson, S., Hurley, J. R., Bailes, M., & Broekgaarden, F. 2021, *MNRAS*, 504, 3682
- Chattopadhyay, D., Stevenson, S., Hurley, J. R., Rossi, L. J., & Flynn, C. 2020, *MNRAS*, 494, 1587
- Cheng, K. S., Ho, C., & Ruderman, M. 1986a, *The Astrophysical Journal*, 300, 500
- . 1986b, *The Astrophysical Journal*, 300, 522
- Chomiuk, L., & Povich, M. S. 2011, *AJ*, 142, 197
- Cocke, W. J., Disney, M. J., & Taylor, D. J. 1969, *Nature*, 221, 525
- Cordes, J. M., & Lazio, T. J. W. 2002, *arXiv e-prints*, astro
- Dewey, R. J., Taylor, J. H., Weisberg, J. M., & Stokes, G. H. 1985, *ApJ*, 294, L25
- Dirson, L., Pétri, J., & Mitra, D. 2022, *A&A*, 667, A82
- Eckner, C., Hou, X., Serpico, P. D., et al. 2018, *The Astrophysical Journal*, 862, 79
- Evans, N. J., Kim, J.-G., & Ostriker, E. C. 2022, *ApJ*, 929, L18
- Faucher-Giguère, C.-A., & Kaspi, V. M. 2006, *ApJ*, 643, 332
- Fermi-LAT Collaboration. 2017, *arXiv e-prints*, arXiv:1705.00009
- Flynn, C., Sommer-Larsen, J., & Christensen, P. R. 1996, *MNRAS*, 281, 1027
- Fritz, G., Henry, R. C., Meekins, J. F., Chubb, T. A., & Friedman, H. 1969, *Science*, 164, 709
- Fruchter, A. S., Stinebring, D. R., & Taylor, J. H. 1988, *Nature*, 333, 237
- Graber, V., Ronchi, M., Pardo-Araujo, C., & Rea, N. 2023, *arXiv e-prints*, arXiv:2312.14848
- Gullón, M., Pons, J. A., Miralles, J. A., et al. 2015, *MNRAS*, 454, 615
- Gunn, J. E., & Ostriker, J. P. 1970, *ApJ*, 160, 979
- Hakobyan, H., Philippov, A., & Spitkovsky, A. 2023, *ApJ*, 943, 105
- Halpern, J. P., & Holt, S. S. 1992, *Nature*, 357, 222
- Han, J. L., Wang, C., Wang, P. F., et al. 2021, *Research in Astronomy and Astrophysics*, 21, 107
- Hobbs, G., Lorimer, D. R., Lyne, A. G., & Kramer, M. 2005, *MNRAS*, 360, 974
- Hooper, D., & Mohlabeng, G. 2016, *Journal of Cosmology and Astroparticle Physics*, 2016, 049
- Hulse, R. A., & Taylor, J. H. 1975, *ApJ*, 195, L51
- Hurley, J. R., Pols, O. R., & Tout, C. A. 2000, *MNRAS*, 315, 543
- Hurley, J. R., Tout, C. A., & Pols, O. R. 2002, *MNRAS*, 329, 897
- Hurley, J. R., Tout, C. A., Wickramasinghe, D. T., Ferrario, L., & Kiel, P. D. 2010, *MNRAS*, 402, 1437
- Igoshev, A. P. 2020, *MNRAS*, 494, 3663
- Igoshev, A. P., Chruslinska, M., Dorozsmai, A., & Toonen, S. 2021, *MNRAS*, 508, 3345
- Igoshev, A. P., Frantsuzova, A., Gourgouliatos, K. N., et al. 2022, *MNRAS*, 514, 4606
- Johnston, S., Smith, D. A., Karastergiou, A., & Kramer, M. 2020, *MNRAS*, 497, 1957
- Kalopotharakos, C., Brambilla, G., Timokhin, A., Harding, A. K., & Kazanas, D. 2018, *ApJ*, 857, 44
- Kalopotharakos, C., Harding, A. K., Kazanas, D., & Wadiasingh, Z. 2019, *ApJ*, 883, L4
- Kalopotharakos, C., Wadiasingh, Z., Harding, A. K., & Kazanas, D. 2022, *ApJ*, 934, 65
- Kapil, V., Mandel, I., Berti, E., & Müller, B. 2023, *Mon. Not. Roy. Astron. Soc.*, 519, 5893
- Kiel, P. D., Hurley, J. R., Bailes, M., & Murray, J. R. 2008, *MNRAS*, 388, 393
- Kniffen, D. A., Hartman, R. C., Thompson, D. J., Bignami, G. F., & Fichtel, C. E. 1974, *Nature*, 251, 397
- Kramer, M., et al. 2021, *Phys. Rev. X*, 11, 041050
- Kroupa, P. 2001, *Mon. Not. Roy. Astron. Soc.*, 322, 231
- Lattimer, J. M., & Schutz, B. F. 2005, *ApJ*, 629, 979
- Licquia, T. C., & Newman, J. A. 2015, *ApJ*, 806, 96
- Lorimer, D. R., & Kramer, M. 2004, *Handbook of Pulsar Astronomy*, Vol. 4
- Lorimer, D. R., Faulkner, A. J., Lyne, A. G., et al. 2006, *MNRAS*, 372, 777
- Lyne, A. G., & Lorimer, D. R. 1994, *Nature*, 369, 127
- Lyne, A. G., Manchester, R. N., & Taylor, J. H. 1985, *MNRAS*, 213, 613
- Makarenko, E. I., Igoshev, A. P., & Kholtygin, A. F. 2021, *MNRAS*, 504, 5813
- Malofeev, V. M., & Malov, O. I. 1997, *Nature*, 389, 697
- Manchester, R. N., Hobbs, G. B., Teoh, A., & Hobbs, M. 2005, *Astron. J.*, 129, 1993
- Manchester, R. N., Lyne, A. G., Camilo, F., et al. 2001, *MNRAS*, 328, 17
- Mandel, I., & Igoshev, A. P. 2023, *Astrophys. J.*, 944, 153
- Mandel, I., & Müller, B. 2020, *Mon. Not. Roy. Astron. Soc.*, 499, 3214
- Mann, H. B., & Whitney, D. R. 1947, *The Annals of Mathematical Statistics*, 18, 50
- McCann, A. 2015, *ApJ*, 804, 86
- Miyamoto, M., & Nagai, R. 1975, *PASJ*, 27, 533
- Nather, R. E., Warner, B., & Macfarlane, M. 1969, *Nature*, 221, 527
- Navarro, J. F., Frenk, C. S., & White, S. D. M. 1997, *ApJ*, 490, 493
- Oegelman, H., Finley, J. P., & Zimmerman, H. U. 1993, *Nature*, 361, 136
- Ośłowski, S., Bulik, T., Gondek-Rosińska, D., & Belczyński, K. 2011, *MNRAS*, 413, 461
- Paczynski, B. 1990, *ApJ*, 348, 485
- Padmanabh, P. V., Barr, E. D., Sridhar, S. S., et al. 2023, *arXiv e-prints*, arXiv:2303.09231
- Pétri, J. 2011, *MNRAS*, 412, 1870
- . 2012, *MNRAS*, 424, 605
- Pierbattista, M., Grenier, I. A., Harding, A. K., & Gonthier, P. L. 2012, *A&A*, 545, A42
- Pletsch, H. J., et al. 2013, *Astrophys. J. Lett.*, 779, L11
- Ploeg, H., Gordon, C., Crocker, R., & Macias, O. 2017, *Journal of Cosmology and Astroparticle Physics*, 2017, 015
- Ploeg, H., Gordon, C., Crocker, R., & Macias, O. 2020, *J. Cosmology Astropart. Phys.*, 2020, 035
- Plummer, H. C. 1911, *MNRAS*, 71, 460
- Popov, S. B., Pons, J. A., Miralles, J. A., Boldin, P. A., & Posselt, B. 2010, *MNRAS*, 401, 2675
- Popov, S. B., & Turolla, R. 2012, *Ap&SS*, 341, 457
- Riley, J., Agrawal, P., Barrett, J. W., et al. 2022, *ApJS*, 258, 34
- Romani, R. W. 1996, *The Astrophysical Journal*, 470, 469
- Ronchi, M., Graber, V., Garcia-Garcia, A., Rea, N., & Pons, J. A. 2021, *ApJ*, 916, 100
- Rossi, L. 2015, *Astronomy and Computing*, 12, 11

- Rudak, B., & Ritter, H. 1994, *MNRAS*, 267, 513
- Ruiter, A. J., Ferrario, L., Belczynski, K., et al. 2019, *MNRAS*, 484, 698
- Sana, H., de Mink, S. E., de Koter, A., et al. 2012, *Science*, 337, 444
- Schneider, F. R. N., Ohlmann, S. T., Podsiadlowski, P., et al. 2019, *Nature*, 574, 211
- Sengar, R., Bailes, M., Balakrishnan, V., et al. 2023, *MNRAS*, arXiv:2302.00255
- Smith, D. A., Bruel, P., Cognard, I., et al. 2019, *ApJ*, 871, 78
- Smith, D. A., Abdollahi, S., Ajello, M., et al. 2023, *ApJ*, 958, 191
- Song, Y., Paglione, T. A. D., Tan, J., Lee-Georgescu, C., & Herrera, D. 2023, *MNRAS*, 524, 5854
- Stevenson, S., Sampson, M., Powell, J., et al. 2019, *ApJ*, 882, 121
- Stevenson, S., Vigna-Gómez, A., Mandel, I., et al. 2017, *Nature Commun.*, 8, 14906
- Stollman, G. M. 1987, *A&A*, 178, 143
- Szary, A., Zhang, B., Melikidze, G. I., Gil, J., & Xu, R.-X. 2014, *ApJ*, 784, 59
- Tabassum, S., & Lorimer, D. 2024, in *American Astronomical Society Meeting Abstracts*, Vol. 243, *American Astronomical Society Meeting Abstracts*, 438.03
- Takata, J., Wang, Y., & Cheng, K. S. 2011, *ApJ*, 726, 44
- Tauris, T. M., & Manchester, R. N. 1998, *MNRAS*, 298, 625
- Tauris, T. M., Sanyal, D., Yoon, S. C., & Langer, N. 2013, *A&A*, 558, A39
- Taylor, J. H., & Manchester, R. N. 1977, *ApJ*, 215, 885
- Thompson, D. J., Arzoumanian, Z., Bertsch, D. L., et al. 1992, *Nature*, 359, 615
- Tumer, O. T., Long, J., Oneill, T., et al. 1984, *Nature*, 310, 214
- Verbunt, F., Igoshev, A., & Cator, E. 2017, *A&A*, 608, A57
- Vigna-Gómez, A., Neijssel, C. J., Stevenson, S., et al. 2018, *Monthly Notices of the Royal Astronomical Society*, 481, 4009
- Vivekanand, M., & Narayan, R. 1981, *Journal of Astrophysics and Astronomy*, 2, 315
- Watters, K. P., Romani, R. W., Weltevrede, P., & Johnston, S. 2009, *ApJ*, 695, 1289
- Wijnands, R., & van der Klis, M. 1998, *Nature*, 394, 344
- Willcox, R., Mandel, I., Thrane, E., et al. 2021, *Astrophys. J. Lett.*, 920, L37
- Yao, J. M., Manchester, R. N., & Wang, N. 2017, *ApJ*, 835, 29
- Ye, C. S., Kremer, K., Chatterjee, S., Rodriguez, C. L., & Rasio, F. A. 2019, *ApJ*, 877, 122
- Ye, C. S., Kremer, K., Ransom, S. M., & Rasio, F. A. 2024, *ApJ*, 961, 98